Flexible Transition State Theory for a Variable Reaction Coordinate: Analytical Expressions and an Application

Struan Robertson

Accelrys, 230/250 The Quorum, Barnwell Rd., Cambridge, CB5 8RE, U.K.

Albert F. Wagner

Argonne National Laboratory, Argonne, Illinois 60439

David M. Wardlaw*

Department of Chemistry, Queen's University, Kingston, Ontario, Canada K7L 3N6

Received: May 4, 2001; In Final Form: September 20, 2001

Completely general canonical and microcanonical (energy-resolved) flexible transition state theory (FTST) rate constant expressions for an arbitrary choice of reaction coordinate have recently been derived [Robertson et al. *J. Chem. Phys.* **2000**, *113*, 2648.] by the present authors. The rate expressions apply to any definition of the separation distance between fragments in a barrierless recombination (or dissociation) that is held fixed during hindered rotations at the transition state, and to any combination of fragment structure (atom, linear top, nonlinear top). The minimization of the rate constant with respect to this definition can be regarded as optimizing the reaction coordinate within a canonical or microcanonical framework. The expressions are analytic, with the exception of a configuration integral whose evaluation generally requires numerical integration over an integrand which depends on internal angles (from one to five depending on the fragment structures). The primary component of the integrand is the determinant of the inverse G-matrix associated with the external rotations and the relative internal rotation of the fragments. In this paper, we derive closed-form, analytic expressions for the inverse G-matrix determinant for all combinations of fragment top types for an arbitrary reaction coordinate definition entirely in terms of kinetic energy matrix elements for a centers-of-mass reaction coordinate. For a model potential for $CFH_2 + H$, the effect of optimizing the reaction coordinate definition is displayed, and the optimized coordinate is compared to the traditional center-of-mass definition at the canonical level. The associated rate constant is about a factor of 20% to 45% lower than that obtained using a centers-of-mass reaction coordinate.

1. Introduction

Reactions whose transition states or "bottlenecks" are characterized by large amplitude motion constitute a large and important class of chemical processes. This situation most commonly arises for recombination of molecular radicals, or the reverse process of single-bond fission, for which there is no (pronounced) potential barrier for the formation of a parent molecule from a pair of constituent molecular fragments. Such "barrierless" reactions are commonplace, particularly in combustion, atmospheric, and interstellar processes. Barrierless reactions are not confined to radical association/dissociation but include bimolecular reactants yielding a pair, or several pairs, of molecular products via a collision complex having a purely attractive potential in some or all arrangement channels, including the reactant channel. Despite ongoing advances in the implementation of classical trajectories and quantum dynamics, statistical theories remain the most widely used approach for modeling reaction rate coefficients. The accurate incorporation of large amplitude motion into statistical theories of reaction kinetics is essential if such theories are to be relied upon for predictions, for interpretation of measurements, and for development of chemical intuition about "floppy" transition states. This endeavor has been, and continues to be, the subject of substantial theoretical attention, e.g., refs 1−5.

Here, we present further developments for accurately incorporating such large amplitude motion within a variational transition state theory (VTST) framework. This paper will deal exclusively with flexible transition state theory (FTST) with a variable reaction coordinate (VRC). FTST-VRC is a version of VTST designed specifically to handle large amplitude motion. The FTST component, originally developed by Wardlaw and Marcus,[6] replaces a quantum mechanical accounting of restricted types of large amplitude motion with a classical accounting of any type of such motion. The VRC component, originally developed by Klippenstein,[7−9] exploits the fact that a reaction coordinate (RC) about which large amplitude motion is executed can itself be variationally selected under the same rate constant minimization principle that animates all VTST theories. All transition state theories of reaction dynamics have a dividing surface (DS) orthogonal to the RC that separates reactants and products. The variational principle is based on the fact that the best DS is the one which minimizes the statistical (canonical or microcanonical) reactive flux. Before the VRC development, that minimization involved optimizing the placement of the DS

* To whom correspondence should be addressed. Fax: 613 533-6669. E-mail: david@chem.queensu.ca.

10.1021/jp0116858 CCC: $22.00
Published on Web 02/16/2002

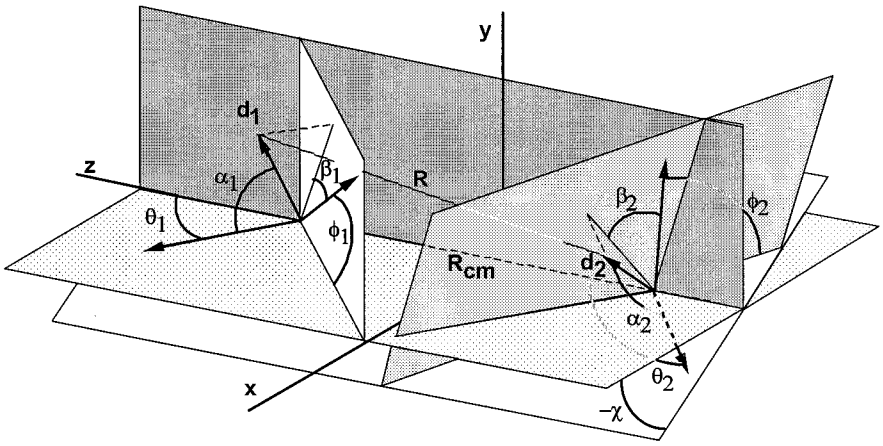

Figure 1. Relative orientation of principal axis coordinate systems on each reactant with respect to the center of mass coordinate system of the collision system as a whole. Within the coordinate system of each reactant, the pivot point displacement vector $\mathbf{d}_i$ is indicated.

along the RC. In the original Wardlaw−Marcus FTST[10] the RC was restricted to be the separation of the centers-of-mass of the fragments, R_{cm}, because a centers-of-mass reaction coordinate (CMRC) provides a natural and simple description of the kinetic energy of the fragments. However, extensive early work by Klippenstein[7,9] showed that the rate constant could be further lowered if the RC was the distance between noncenter-of-mass pivot points about which the fragments executed their large amplitude motion. The optimization of these pivot points on each reactant constitutes a optimization of the RC and one that can noticeably further minimize the calculated FTST reaction rate constant.

This paper is the fourth in a series by the present authors setting out a systematic reformulation of FTST-VRC into a compact, computationally amenable, and physically more transparent form. The computational advantage of our reformulation of FTST becomes especially important when employing "nontraditional" reaction coordinates whose optimization requires numerical effort absent in a sum of states calculation using a single (nonoptimized) definition of the RC, such as a bond coordinate or the centers-of-mass separation. The first paper[11] in the series (hereafter, denoted Paper I) simplified the phase space integrals in FTST, leading to a more physically intuitive form where a steric hindrance factor naturally emerges. The second paper[12] (hereafter, Paper II) began to incorporate the VRC component into the same compact expressions developed in Paper I for R_{cm} as the RC. This incorporation was only for one of five possible cases, the simplest one of an atom reacting with a linear top. (As will be reviewed shortly, the other four cases are atom + nonlinear-top, linear-top + linear-top, linear-top + nonlinear-top, and nonlinear-top + nonlinear-top.) The third paper[13] (hereafter, Paper III) provided a fully general reformulation of FTST-VRC but did not derive the specific formulas necessary to calculate rate constants for each of the five cases. In this paper, these specific formulas are derived and their use is illustrated by a realistic model application.

The structure of the paper is as follows. In Section 2, the theory presented in paper III is briefly reviewed and then specific formulas are systematically derived either in the section or in supporting appendices. In section 3, the application of the current approach to a model of the recombination reaction

$$CFH_2 + H \rightarrow CFH_3 \qquad (1)$$

is developed. This application illustrates the strengths and also the limitations of the FTST-VRC approach as currently implemented and suggests future directions of development. A discussion and conclusions are provided in section 4.

We believe this paper provides a mathematically elegant, computationally tractable, and physically interpretable set of formulas for the incorporation of large amplitude motion in gas-phase reaction kinetics. These formulas have already been implemented in the freeware reaction kinetics program called VariFlex[14] that comes with a manual and instructions. Thus, the approach developed here is accessible without extensive programming.

2. Theory

2.1 Transitional Mode and Reaction Coordinates. For a CMRC, the relative orientation of the fragments is specified by rotating the fragments about "pivot points" located at either end of the line connecting the centers-of-mass of the two fragments. This orientation is conveniently specified by internal Euler angles (Jacobi angles in scattering theory), collectively denoted $\boldsymbol{q}_{cm,int}$. For the case of two nonlinear tops (so that all possible internal angles can be indicated), $\mathbf{q}_{cm,int} = (\theta_1, \phi_1, \theta_2, \phi_2, \chi)$; these angles are identified in Figure 1. For progressively simpler cases, e.g., one nonlinear top is replaced by a linear top, the number of internal angles decreases. The simplest case of an atom + linear top requires only one angle (θ_1) to specify the relative orientation of fragments. Table 1 in Paper III lists all 5 possible cases and the associated angles. Arbitrary pivot points can be characterized by vectors $\mathbf{d}_i (i = 1, 2)$, whose origins are the respective CMs. The associated reaction coordinate R is the line connecting the tips of the two displacement vectors. This situation is also depicted in Figure 1. A point on the reaction coordinate is now located by fixing the value of R. A consequence of such a generalization of the reaction coordinate definition is that R_{cm} now depends on the internal angles and the displacement vectors for a given value of R

$$F = R_{cm}(\mathbf{q}_{cm,int}, \mathbf{d}_1, \mathbf{d}_2; R) \qquad (2)$$

where F is a geometric function representing how R_{cm} depends on $\mathbf{q}_{cm,int}$ and $\mathbf{d}_1$, $\mathbf{d}_2$ while holding a separation distance R fixed.

2.2 FTST Rate Constant Expressions. The generic canonical FTST rate constant expression is

$$k(T) = g_e g_\sigma^{-1} \frac{kT}{h} \frac{Q^\dagger_{cons}(T) Q^\dagger_{tm}(T)}{Q_{react}(T)} e^{-\beta V^\dagger} \qquad (3)$$

Here, Q_{react} is the partition function of the reactants in the center-

of-mass frame; g_e and g_σ are the ratios of transition state to reactant electronic degeneracy factors and symmetry factors, respectively. Q_{cons} is the canonical partition function for the conserved modes. Q_{tm} is the transitional mode partition function for the n transitional/external rotational degrees of freedom, which are assumed separable from the conserved modes in FTST. The '†' on Q_{cons} and Q_{tm} indicates that these quantities are evaluated at that value of the reaction coordinate R, called $R^\dagger$, which minimizes their product at the given temperature, i.e., minimizes the numerator of the rate constant expression in eq 3. $V^\dagger$ denotes the minimum potential energy consistent with the fragments being separated by $R^\dagger$ for a particular choice of RC definition. That is, the configuration associated with $V^\dagger$ is a 'point' on the minimum energy path (MEP), where a point is a set of Cartesian coordinates $\mathbf{r}_{i,MEP}$ specifying the positions of all atoms. Let the particular MEP point associated with a particular RC definition and with a particular RC value ($R^\dagger$) be $\mathbf{r}'_{i,MEP}$. Then we can write $V^\dagger = V_{MEP}(\mathbf{r}'_{i,MEP})$. The factor $e^{-\beta V^\dagger}$ indicates that reactants and transition state have a common energy origin and that potential energy functions appearing in $Q^\dagger_{cons}$ and $Q^\dagger_{tm}$ are implicitly evaluated with respect to $V^\dagger$.

Standard expressions are available for Q_{cons}, and so it will not be discussed further. In Paper III, we showed that Q_{tm} for a variable RC can be expressed as a configuration integral

$$Q^\dagger_{tm}(\beta) = 8\pi^2\left(\frac{2\pi}{\beta h^2}\right)^{n/2}\int d\mathbf{q}_{cm,int}\,|\mathbf{A}_r|^{1/2}\,e^{-\beta\Delta V_{tr}(\mathbf{q}_{cm,int},\,R^\dagger)} \quad (4)$$

A_r is the (reduced) kinetic energy matrix, commonly called the inverse G-matrix, associated with the generalized velocities for the n transitional/external modes when the velocity along the RC (the $(n+1)^{st}$ degree of freedom) is constrained to be zero. It is obtained by reducing the full $(n+1)\times(n+1)$ A-matrix by removing its $(n+1)^{st}$ row and $(n+1)^{st}$ column.

$\Delta V_{tr} = V_{tr} - V^\dagger$ is the transitional mode potential evaluated with respect to $V^\dagger$.

The corresponding microcanonical expression is

$$k(E) = g_e g_\sigma^{-1}\frac{N^\dagger(E)}{h\rho_{react}(E)} \quad (5)$$

where

$$N^\dagger(E) = \int_0^{E-V^\dagger} d\epsilon\;\rho_{cons}(\epsilon, R^\dagger) g\,\frac{8\pi^2}{\Gamma\left(\frac{n}{2}+1\right)}\left(\frac{2\pi}{h^2}\right)^{n/2}\times$$

$$\int\cdots\int d\mathbf{q}_{cm,int}\,|\mathbf{A}_r|^{1/2}\,(E - V^\dagger - \epsilon - \Delta V_{tr}(\mathbf{q}_{cm,int}, R^\dagger))^{n/2}\times$$

$$\times\, u(E - V^\dagger - \epsilon - \Delta V_{tr}(\mathbf{q}_{cm,int}, R^\dagger)) \quad (6)$$

and u is the Heaviside function. In eqs 4 and 6, the dependence of the determinant on the variables of integration and on R is implicit.

The determinant in eqs 4 and 6 can be expressed as

$$|\mathbf{A}_r| = |\mathbf{A}_r^0 + \delta\mathbf{A}_r| \quad (7)$$

$\mathbf{A}_r^0$ is the reduced kinetic energy matrix for a CMRC and $\delta\mathbf{A}_r$ accounts for the motion of the fragments about pivot points displaced from the fragments' centers-of-mass. The general form of the matrix elements for $\mathbf{A}_r^0$ and $\delta\mathbf{A}_r$ is derived in Paper III. $\delta\mathbf{A}_r$ has a particularly simple form and is conveniently expressed in terms the function F (eq 3)

$$\delta\mathbf{A}_r = \begin{bmatrix}\mathbf{0}_{3\times3} & \mathbf{0}_{3\times m}\\ \mathbf{0}^T_{m\times3} & \mu[(\nabla F)(\nabla F)^T]_{m\times m}\end{bmatrix} \quad (8)$$

where $m = n - 3$ is the number of transitional modes, $\mathbf{0}_{3\times3}$ is the 3×3 null matrix, $\mathbf{0}_{3\times m}$ is the $3\times m$ null matrix, and ∇F is the gradient (column) vector

$$\nabla F = \nabla_{\mathbf{q}_{cm,int}} F = \left(\frac{\partial F}{\partial q_{cm,int,1}}, ..., \frac{\partial F}{\partial q_{cm,int,m}}\right) \quad (9)$$

Introducing eq 8 in eq 7 followed by the manipulations described in detail in Paper III yields

$$|\mathbf{A}_r|^{1/2} = |\mathbf{A}_r^0|^{1/2}(F)\{1 + \mu[\sum_{i=4}^{n}(\nabla F)_i^2\,(G_r^0)_{ii} + 2\sum_{i=4}^{n-1}\sum_{j=i+1}^{n}(\nabla F)_i(\nabla F)_j\,(G_r^0)_{ij}]\} \quad (10)$$

Here $\mathbf{A}_r^0(F)$ has exactly the same form as the reduced kinetic energy matrix for a centers-of-mass reaction coordinate (CMRC) but with F substituted for R_{cm}. $\mathbf{G}_r^0$ is the corresponding reduced version of $\mathbf{G}^0$ obtained by removal of the last row and last column from the latter, i.e., by removal of matrix elements relating to motion along the CMRC. $\mathbf{G}^0$ is the inverse of $\mathbf{A}^0$ and is defined by

$$2T = \mathbf{P}^T_{cm}\,\mathbf{G}^0\,\mathbf{P}_{cm} = \dot{\mathbf{Q}}^T_{cm}\,\mathbf{A}^0\,\dot{\mathbf{Q}}_{cm} \quad (11)$$

where $\dot{\mathbf{Q}}^T_{cm} = (\omega_x, \omega_y, \omega_z, \dot{\mathbf{q}}_{cm,int}, \dot{R}_{cm})$ is the generalized velocity vector [as defined in eq 11 of Paper III] and $\mathbf{P}_{cm} = \mathbf{A}^0\dot{\mathbf{Q}}_{cm}$. In Paper III, we established that $\mathbf{G}_r^0\mathbf{A}_r^0 = \mathbf{1}$. Thus

$$(G_r^0)_{ij} = (-1)^{i+j}\frac{|(\mathbf{A}_r^0)^{ij}|}{|\mathbf{A}_r^0|} \quad (12)$$

where $|(\mathbf{A}_r^0)^{ij}|$ is the ij minor determinant of $\mathbf{A}_r^0$.

To evaluate the canonical or microcanonical FTST-VRC rate constant one must evaluate the configuration integral in the expressions for $Q^\dagger_{tm}(T)$ [eq 4] or $N^\dagger(E)$ [eq 6], respectively. Both evaluations require knowledge of the case-specific form of $|\mathbf{A}_r|$ whose general form is given by eq 10. The next subsection provides analytic results for the matrix $\mathbf{A}_r^0$, its determinant, and the required elements of the $\mathbf{G}_r^0$ for cases 1−5 ($n = 4, 5, ..., 8$). The following subsection derives an analytic expression for the function F [eq 2] for case 5 ($n = 8$). We note that these configuration integrals require knowledge of V_{tr}, in addition to $|\mathbf{A}_r|$ and F. V_{tr} depends on the details of the potential energy surface and thus varies from application to application. However, $|\mathbf{A}_r|$ and F have invariant forms for each of cases 1−5, i.e., for each combination of top types; the only system-dependent aspect within a particular case is the moments of inertia of the top(s). Because the determination of the rate constant with an optimization of the value and definition of the reaction coordinate requires repeated evaluations of Q_{tm} or $N(E)$, our formulation offers distinct simplifications in the construction of computer code as well as significant computational efficiencies over original FTST. All of the results described in the next two subsections have been incorporated in the VariFlex software package.[14]

2.3 Analytic Expressions for Kinetic Energy Matrix Elements and Determinant. Analytic expressions for $\mathbf{A}_r^0$, $|\mathbf{A}_r^0|$, and the required elements of $\mathbf{G}_r^0$ are listed in Appendix A in subsections A.1 − A.5 for cases 1−5, respectively. They are functions of the internal angles $\mathbf{q}_{cm,int}$ and also depend on the moments of inertia of fragment top(s) and on the moment of inertia for 'external' rotation of the fragments' centers-of-mass about the overall center-of-mass. All results were obtained by manual simplification of output generated by algebraic manipulation software.[22] For the simpler cases, (i.e. atom + linear top and linear top + linear top) the elements of $\mathbf{A}_r^0$ were obtained by writing the Cartesian components $\mathbf{r}_i = (x_i, y_i, z_i)$ of each the N atoms in terms of $(\mathbf{q}_{cm,int}, R_{cm})$, substituting in

$$2T = \sum_{i=1}^{N} m_i \dot{\mathbf{r}}_i \cdot \mathbf{r}_i + 2\omega \cdot \sum_{i=1}^{N} m_i \mathbf{r}_i \times \dot{\mathbf{r}}_i + \omega^T \cdot \mathbf{I} \cdot \omega \quad (13)$$

and regrouping terms to obtain an expression in the form of eq 11. For those cases that involve nonlinear asymmetric tops, this simple approach proved to be intractable leading to large equations that could not easily be reduced to terms involving the principal moments of inertia of fragments. Instead direct manipulation of the inertia tensors was used to generate overall inertia components, internal rotatation energies and coriolis terms. Further details are provided by eqs 8−16 of Paper III. The G-matrix elements are determined via eq 12.

For nonlinear top fragments (cases 2, 4, and 5), we present results in Appendix A for the most general situation of an asymmetric top. Note that all azimuthal angle (ϕ_1, ϕ_2) dependence in $\mathbf{A}_r^0$ is contained in trigonometric combinations of the two moments I_{ib} and I_{ic}. In the convention of this paper, these two moments become identical as the asymmetric top goes to a symmetric top. Careful consideration of expressions given in appendix A shows that, in the limit that a top becomes symmetric, all azimuthal angle dependence of the matrix elements of $\mathbf{A}_r^0$ vanishes. In the symmetric top + symmetric top limit, the matrix in Appendix A.5 is identical to the **A** matrix in Table 1 of Paper I.

Many of the terms in the G-matrix element expressions in Appendix A contain one of the following factors: $(\sin\theta_1)^{-1}$, $(\sin\theta_2)^{-1}$, $(\sin\theta_1 \sin\theta_2)^{-1}$, or the square of one of these factors. Such G-matrix elements are singular when θ_1 or θ_2 is 0 or π, i.e., at either end of the allowed range. However, the expression for $|\mathbf{A}_r^0|$ always contains a factor of $\sin^2\theta_1$ and/or $\sin^2\theta_2$, depending on the case [see Appendix A], which cancels any inverse sine factors in the G-matrix elements appearing in the expression for $|\mathbf{A}_r|$ [eq 10]. Consequently, the integrands in the transitional mode partition function expression [eq 4] and the microcanonical sum of states expression [eq 6] are always mathematically well-behaved.

2.4 Derivation of *F*. F is the function which relates R_{cm} to the distance R between the pivot points of the two reactants. Let the vector $\mathbf{d}_i$ locate the position of the pivot point of the ith reactant relative to its center of mass, as in Figure 1. R is the distance between the tips of $\mathbf{d}_1$ and $\mathbf{d}_2$, whereas R_{cm} is the distance between the origins of $\mathbf{d}_1$ and $\mathbf{d}_2$. $\mathbf{d}_i$ is defined in terms of the principal axis coordinate system centered on each reactant as in Figure 1, i.e., $\mathbf{d}_i$ is characterized by a length d_i, and polar and azimuthal angles α_i and β_i (as seen in Figure 1). Because the relative orientation of the internal axes are characterized by the Euler angles θ_1, ϕ_1, θ_2, ϕ_2, and χ, F is a function of those angles and the derivative of that dependence is needed in the construction of $|\mathbf{A}_r|$ via eq 10. In general, F can be written as

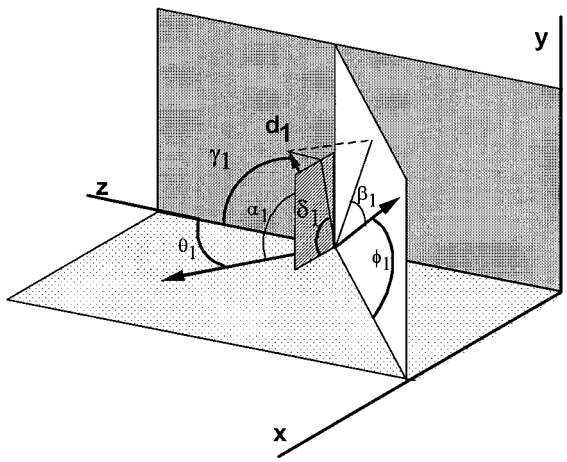

Figure 2. Definition of γ_1 and δ_1 in an expanded view of the coordinate system of the first reactant in Figure 1.

$$F = R_{cm}(\theta_1, \phi_1, \theta_2, \phi_2, \chi, d_1, \alpha_1, \beta_1, d_2, \alpha_2, \beta_2; R) \quad (14)$$

An explicit expression is derived below for case 5 (two nonlinear tops) from which the corresponding expressions for Cases 1−4 are readily obtained by systematic simplification.

It is convenient that the angular orientation of $\mathbf{d}_i$ be first expressed in terms of the polar angle γ_i and the azimuthal angle δ_i with respect to the collision coordinate system translated to the center of mass of the ith reactant. These angles are illustrated in Figure 2 for reactant 1.

The derivation of F begins with the vector relation

$$\mathbf{R} = \mathbf{R}_{cm} + \mathbf{d}_2 - \mathbf{d}_1 \quad (15)$$

The magnitude of R is thus given by

$$\begin{aligned} R^2 &= \mathbf{R} \cdot \mathbf{R} \\ &= (\mathbf{R}_{cm} + \mathbf{d}_2 - \mathbf{d}_1) \cdot (\mathbf{R}_{cm} + \mathbf{d}_2 - \mathbf{d}_1) \\ &= {R_{cm}}^2 + {d_1}^2 + {d_2}^2 + 2\mathbf{R}_{cm} \cdot (\mathbf{d}_2 - \mathbf{d}_1) - 2\mathbf{d}_2 \cdot \mathbf{d}_1 \\ &= {R_{cm}}^2 + {d_1}^2 + {d_2}^2 + 2R_{cm}(d_2 \cos\gamma_2 - d_1 \cos\gamma_1) \\ &\quad -2d_1 d_2[\cos\gamma_1 \cos\gamma_2 + \sin\gamma_1 \sin\gamma_2 \cos(\delta_1 - \delta_2)] \end{aligned} \quad (16)$$

where the square brackets enclose an expression for the cosine of the angle between $\mathbf{d}_1$ and $\mathbf{d}_2$, if these two vectors where translated along the z axis to a common origin. Solving the quadratic in R_{cm} gives

$$\begin{aligned} F = d_1 \cos\gamma_1 - d_2 \cos\gamma_2 \pm (R^2 - {d_1}^2 - {d_2}^2 + \\ {d_1}^2 \cos^2\gamma_1 + {d_2}^2 \cos^2\gamma^2 + 2d_1 d_2 [\cos\gamma_1 \cos\gamma_2 + \\ \sin\gamma_1 \sin\gamma_2 \cos(\delta_1 - \delta_2)])^{1/2} \end{aligned} \quad (17)$$

This expression reduces to $F = R$ as d_1, $d_2 \rightarrow 0$. It is also consistent with the result derived in Paper II for the simplest case of a linear top plus atom if reactant 1 is the atom. Equation 17 indicates that, in general, there are two possible values of F for a given R, a situation which is physically meaningful only if both values of F are positive. Conditions determining whether there is one or two values of F and the corresponding physical

interpretation are discussed later below for the simplest case of an atom + linear top.

The above solution for F [eq 17] still requires an explicit relationship between (γ_i, δ_i) and (α_i, β_i, θ_i, ϕ_i, χ). The necessary relationships are derived in Appendix B for the case of two nonlinear tops. Substitution of eqs B1, B5, B6 into eq 17 yields an explicit closed-form expression for F depending on the variables indicated on the right-hand side of eq 14. The derivatives of this expression with respect to θ_1, ϕ_1, θ_2, ϕ_2, and χ provide the components of the gradient of F appearing in eq 10.

If either reactant is a linear top or an atom, then the expressions in Appendix B must be modified. In the case of a linear top, the orientation of the internal x- and y-axes cannot be fixed in the plane perpendicular to the internal z-axis because of the rotational symmetry of the linear top about its symmetry axis. Consequently, ϕ and β for that reactant cannot be defined. Without a β, α cannot be used to locate **d** except along the z-axis, i.e., $\alpha = 0$ or π. Thus for a linear top, the dependency on ϕ and β in expressions eqs B.4, B.8, and B.9 vanishes because the terms involving these two angles always have a sin α prefactor. For an atom, there is no internal coordinate system that can be defined independently of the other reactant. **d** cannot be oriented in space in a way uniquely associated to the atom and therefore must be 0.

The expression for F is physically meaningful only if the argument of the square root term (third term) in eq 17

$$R^2 - {d_1}^2 - {d_2}^2 + {d_1}^2 \cos^2 \gamma_1 + {d_2}^2 \cos^2 \gamma_2 + 2d_1d_2[\cos \gamma_1 \cos \gamma_2 + \sin \gamma_1 \sin \gamma_2 \cos(\delta_1 - \delta_2)] \quad (18)$$

is positive or zero. It is straightforward to show that this is so when $R \geq d_1 + d_2$. For $R < d_1 + d_2$, expression 18 is positive for restricted ranges of the angles (θ_1, ϕ_1, θ_2, ϕ_2, χ) for fixed values of (d_1, α_1, β_1, d_2). This is easily illustrated in the simplest case of a linear top + atom for which θ_1 is the sole Euler angle. With $\mathbf{d}_2 = 0$, eq 17 becomes

$$F = d_1 \cos \gamma_1 \pm (R^2 - {d_1}^2 + {d_1}^2 \cos^2 \gamma_1)^{1/2} \quad (19)$$

From the discussion in the preceding paragraph about a linear top fragment, $\alpha_1 = 0$ or π in this case. Substitution of cos $\alpha_1 = \pm 1$ in eq B1 yields cos $\gamma_1 = \pm$cos θ_1 and thus

$$F = \pm d_1 \cos \theta_1 \pm (R^2 - {d_1}^2 + {d_1}^2 \cos^2 \theta_1)^{1/2} = \pm d_1 \cos \theta_1 \pm (R^2 - {d_1}^2 \sin^2 \theta_1)^{1/2} \quad (20)$$

Clearly the argument of the square root in eq 20 is always positive if $R > d_1$ but if $R < d_1$, it is positive only if $R^2 > {d_1}^2 \sin^2 \theta_1$ which sets the maximum value of θ_1 at $(\theta_1)_{max} = \sin^{-1}(R/d_1)$. Thus for a linear top + atom with $R < d_1$, the range of integration over θ_1 in the configuration integral in eq 4 or 6 must be restricted to (0, $(\theta_1)_{max}$) instead of using the full range (0, π). For $\theta_1 < (\theta_1)_{max}$, there are two positive values of F for a given θ_1 and R, a larger value F_+ obtained by choosing the positive sign for the second term in eq 19 or 20 and a smaller one F_- corresponding to the negative sign. The relative configurations of fragments associated with F_+ and F_- are different and correspond to different values of the angle θ_1' between $\mathbf{d}_1$ and **R**. As θ_1 (angle between $\mathbf{d}_1$ and $\mathbf{R}_{cm}$) increases from 0 to $(\theta_1)_{max}$), θ_1' takes on its entire range of values from 0 to π, with each value of θ_1 giving rise to two values of θ_1'. Since a physically correct transition state dividing surface must include all relative angular orientations of the fragments, the rate constant, for the $R < d_1$ case, must be defined as $k(R) = k_+(R) + k_-(R)$, where $k_\pm(R)$ are obtained by using $F_\pm$ in eq 4 or eq 6. In practice, the values of d_1 and R in the vicinity of typical flexible transition state values are such that choosing the negative sign in eq 19 or 20 yields values of $R_{cm} = F_-$ which correspond to locating the approaching atom in the vicinity of one end or the other of the linear fragment (depending on $\alpha_1 = 0$ or π). Such configurations are generally highly repulsive and the associated large values of the interaction potential lead to relatively small values of the configuration integral. Thus, for a physically reasonable series of R and d_1 values such that $R < d_1$, the k_+ rate constant will greatly exceed its k_- counterpart and one expects that the k_- values will be sufficiently small as to be irrelevant, so that $k(R) \approx k_+(R)$. For the other four cases, a closed form determination of the limits on the ranges of the euler angles is not possible. Consider for example, the least complex of these is the nonlinear top + atom case (with $\mathbf{d}_2 = 0$). For $R < d_1$ one would have to determine $(\theta_1)_{max}(\phi)$ for each value of ϕ by finding the root of the argument of the square root term in eq 19 with cos $\gamma_1 =$ cos α_1 cos $\theta_1 -$ sin α_1 sin θ_1 cos($\beta_1 + \phi_1$) [eq B1]. This is a transcendental equation in θ_1. Rather than solving such transcendental equations numerically and using the results to restrict the integration ranges, we incorporate this situation directly in the numerical evaluation of the integral in eq 4 or 6. The full range of the Euler angles is employed in our integration schemes and the argument of the square root term in eq 17 is expressed in terms of Euler angles via eqs B1, B5, and B6. Each integration point in a quadrature or Monte Carlo numerical integration specifies a set of Euler angles. If the argument of the square root term is negative for a particular integration point, the corresponding value of the integrand is set to zero. If the argument is positive and $R > d_1 + d_2$, a single value of F is determined by selecting the positive sign for the square root term in eq 17; if the argument is positive and $R < d_1 + d_2$, then there are two possible values of F corresponding to the positive and negative signs and $k(R) = k_+(R) + k_-(R)$. This procedure identifies, in an automatic manner, the restrictions imposed on the angular ranges and the two contributions to the rate constant when $R < d_1 + d_2$.

Given the hindering potential V_{tr}, the entire expression for Q_{tm} can be evaluated and, with that, the rate constant. Through F, the final rate constant will have a dependence on d_1, α_1, β_1, d_2, α_2, β_2, and R. Minimization of the rate constant with respect to these parameters optimizes the definition of the reaction coordinate. Simultaneous final minimization of the rate constant along this optimized reaction coordinate gives the best estimate of the rate coefficient. However, local minima in this parameter space can lead to ambiguities as to the correct choice for, and physical significance of, the transition state dividing surface, a situation illustrated by the example in Section 3.

3. Application

The earliest applications of a VRC description have involved pivot point displacements along the bond axes of linear tops.[1,7,9,8] More recent applications have involved optimized pivot points that are not along bond axes.[4,15] To illustrate the comparable flexibility of the approach given above, an application will be presented in this section, in which there is no symmetry axis, namely the recombination H + CFH_2. This example, while realistic in qualitative terms, is not designed to be chemically reliable and no comparison to experiment will be offered. (A chemically reliable study of the H + CF_mH_{3-m}(m = 1, 2, 3) employing ab initio potential energy surfaces is in progress.)

Rather, this example is designed to show the broad implications of an unconstrained pivot point optimization. In this spirit, only the canonical version of the theory is applied and temperatures confined to the range 300−2000 K. Lower or higher temperatures pose no problems for the method except for the anticipated emergence of quantum effects at very low temperatures. The H + CFH_2 example does have a plane of symmetry and the implication of this symmetry element for the implementation of the formalism developed above will be explicitly examined. This consistency check is the reason for choosing this example rather than a case with no symmetry at all (which is equally amenable to the theory in this paper).

The model used for H + CFH_2 has the following characteristics. The isolated CFH_2 geometry is derived from recent ab initio calculations[19] which predict a nonplanar CFH_2 radical. The CFH_2 fragment is assigned the geometry of the isolated radical throughout the region of the transitional mode potential energy surface (PES) controlling the recombination kinetics. The conserved vibrational degrees of freedom are presumed unchanged in character in this region. The dependence of the PES on separation and relative orientation of fragments is represented by nonbonded and bonding interactions. The nonbonded interactions of the attacking H with the F and H atoms on the radical are represented by Lennard-Jones potentials with parameters developed by Mayo et al..[16] The bonding potential between the attacking H atom and the C atom on the radical has a dependence on both the bond length r_{CH} and on the angle of approach. The bond length dependence is represented by a Morse oscillator (V_M) with the usual three parameters: the dissociation energy D_e, the equilibrium bond length r_e, and the beta parameter β_e. The D_e value is determined from the reaction enthalpy at 298 K that can be constructed from the JANAF tables[17] for CH_3F and the NASA tables[18] for CH_2F. This reaction enthalpy is corrected for the harmonic zero point energy using the JANAF frequencies. The r_e value comes from the JANAF tabulation for CH_3F. The β_e value comes from a fit to ab initio calculations of the reaction path.[19] It is about 15% higher than what would be calculated from D_e, r_e, and the relevant harmonic frequency of CH_3F. The angular dependence of the bonding interaction is represented by the square of the cosine of the angle the attacking H makes with the equal splay axis of the radical. That axis passes through the C atom in such a way that the two C−H bonds and the C−F bond of the radical make equal angles with respect to the axis. The ab initio studies,[19] as well as chemical intuition, would suggest that the equal splay axis is approximately the minimum energy path (MEP) of the recombination reaction.

The PES in the region kinetically important for recombination then takes the form

$$V(r_{CH}, \gamma_{CH}, \delta_{CH}) = V_{LJ}(r_{CH}, \gamma_{CH}, \delta_{CH}) + \cos^2(\gamma_{CH})[V_M(r_{CH}) - V_{LJ}(r_{CH}, 0, 0)] \quad (21)$$

where (r_{CH}, γ_{CH}, δ_{CH}) are the spherical polar components of a vector from C to the attacking H, built around the equal splay axis, V_{LJ} is sum of nonbonded interactions assuming a fixed (asymptotic) geometry of the CFH_2, and V_M is the bonding interaction described above. Note that at $\gamma_{CH} = 0$, V becomes the Morse potential V_M. In other words, for this model potential the MEP lies along the equal splay axis and $V_{MEP} = V_M$. Although it is not guaranteed that the actual MEP is coincident with the equal splay axis, tests show that this is a very good approximation. The above form is similar in spirit to the original Wardlaw−Marcus[10] potential proposed in the original applications of FTST. However, it avoids the fitting of effective Morse potentials required by that approach. The resulting potential is certainly realistic but is probably not quantitative and has not been compared to the corresponding Wardlaw−Marcus[10] version.

With this PES for H+ CFH_2, the canonical rate constant versus temperature can be determined from the formalism in the previous sections. The reactants belong to the asymmetric top + atom case ($n = 5$). The canonical rate constant expression is obtained by tailoring the general expression, eq 3, so that fragment 1 is a nonlinear top and fragment 2 is an atom

$$k(T) = g_e g_\sigma^{-1} \frac{kT}{h} \frac{Q^\dagger_{cons}\, Q^\dagger_{tm}}{Q_{trans} Q_{vib,1} Q_{fr,1}} \exp(-V^\dagger/kT) = \frac{1}{4}\frac{kT}{h}\frac{Q^\dagger_{tm}}{Q_{trans}Q_{fr,1}} \exp(-V^\dagger/kT) \quad (22)$$

The second equality is a result of setting $g_e = 1/4$, $g_\sigma = 1$, and $Q^\dagger_{cons} = Q_{vib,1}$ (i.e., CFH_2 conserved mode frequencies are assumed not to vary along reaction coordinate in our model potential for this system). Q_{trans} and $Q_{fr,1}$ are the translational partition function (per unit volume) for relative motion of the fragments and the rotational partition function of the CFH_2 radical, respectively.

The general expression for $Q^\dagger_{tm}$ is given in eq 4 and depends, among other things, on $|\mathbf{A}_r|^{1/2}$. The case specific expression for $|\mathbf{A}_r|^{1/2}$ is obtained by substituting the explicit expressions for $|\mathbf{A}_0|$ and $(G_r^0)_{ij}$ for $n = 5$ from Appendix A.2 in the general expression given by eq 10

$$|\mathbf{A}_r|^{1/2} = (\mu F^2)(I_{1a}I_{1b}I_{1c})^{1/2}\sin\theta_1 \{1 + \mu[(\nabla F)_4^{\,2}\,(G_r^{\,0})_{44} + (\nabla F)_5^{\,2}\,(G_r^{\,0})_{55} + 2(\nabla F)_4(\nabla F)_5\,(G_r^{\,0})_{45}]\}^{1/2} \quad (23)$$

where I_{1a}, I_{1b}, and I_{1c} are the moments of inertia of CFH_2. In general, these moments vary along the reaction coordinate, being determined by the geometry of the fragments at a position along the MEP corresponding to the particular value of the reaction coordinate, R. In our model potential for CFH_2 + H, the geometry of CFH_2 along the reaction coordinate is fixed at that of the isolated radical. Thus, the moments of inertia in eq 23 are constant and equal to their 'asymptotic' values. Introducing eq 23 into eq 4 and setting $\mathbf{q}_{cm,int} = (\theta_1, \phi_1)$ yields

$$Q_{tm}{}^\dagger(\beta) = 8\pi^2\left(\frac{2\pi}{\beta h^2}\right)^{n/2}(I_{1a}I_{1b}I_{1c})^{1/2}\int_0^\pi \sin\theta_1\, d\theta_1 \int_0^{2\pi} d\phi_1\, \mu F^2 \times \{1 + \mu[(\nabla F)_4^{\,2}\,(G_r^{\,0})_{44} + (\nabla F)_5^{\,2}\,(G_r^{\,0})_{55} + 2(\nabla F)_4(\nabla F)_5\,(G_r^{\,0})_{45}]\}^{1/2}\, e^{-\beta\Delta V_{tr}(\theta_1,\phi_1;R^\dagger)} \quad (24)$$

The canoncial rate constant expression (eq 22) becomes, after introducing the above expression for $Q^\dagger_{tm}$, setting $Q_{trans} = (2\pi\mu/\beta h^2)^{3/2}$, setting $Q_{fr,i} = (2\pi/\beta p^2)^{3/2}(I_{1a}I_{ib}I_{ic})^{1/2}$, and allowing the moments of inertia in the numerator and denominator to cancel

$$k(T) = \frac{1}{4}\left(\frac{8kT}{\mu\pi}\right)^{1/2}\exp(-V^\dagger/kT) \times \frac{1}{4\pi}\int_0^\pi \sin\theta_1\, d\theta_1 \int_0^{2\pi} d\phi_1\, F^2 \times \{1 + \mu[(\nabla F)_4^{\,2}\,(G_r^{\,0})_{44} + (\nabla F)_5^{\,2}\,(G_r^{\,0})_{55} + 2(\nabla F)_4(\nabla F)_5\,(G_r^{\,0})_{45}]\}^{1/2}\, e^{-\beta\Delta V_{tr}(\theta_1,\phi_1;R^\dagger)} \quad (25)$$

The case-specific expression for F is obtained by setting $\mathbf{d}_2 =$

0 in eq 17 and inserting eq B1 in eq 17 yielding

$$F = -d_1 Y + [R^2 - d_1^2(1 - Y^2)]^{1/2} \quad (26)$$

where

$$Y = \cos\alpha_1 \cos\theta_1 - \sin\alpha_1 \sin\theta_1 \cos(\beta_1 + \phi_1) \quad (27)$$

The case-specific expressions for the elements of the gradient of F are

$$(\nabla F)_{\theta_1} = \frac{\partial F}{\partial Y}\frac{\partial Y}{\partial \theta_1} = -(\cos\alpha_1 \sin\theta_1 + \sin\alpha_1 \cos\theta_1 \cos(\beta_1 + \phi_1))\frac{\partial F}{\partial Y} \quad (28)$$

$$(\nabla F)_{\phi_1} = \frac{\partial F}{\partial Y}\frac{\partial Y}{\partial \phi_1} = \sin\alpha_1 \sin\theta_1 \sin(\beta_1 + \phi_1)\frac{\partial F}{\partial Y} \quad (29)$$

where

$$\frac{\partial F}{\partial Y} = -d_1 + d_1^2 Y[R^2 - d_1^2(1 - Y^2)]^{1/2} \quad (30)$$

The optimal rate coefficient is obtained by minimizing $Q_{tm}\exp(-V/kT)$ with respect to the value and definition of the reaction coordinate. Because this particular reaction is an example of an asymmetric top plus atom reaction, minimization proceeds in a four parameter space of R, $d = d_1$(radial distance), $\alpha = \alpha_1$(polar angle with respect to principal axis associated with smallest moment of inertia, i.e., the one nearly coincident with the C−F axis of CFH_2), and $\beta = \beta_1$ (azimuthal angle selected so as to be measured from an x axis located in the symmetry plane of CFH_2). In doing the minimization, the integral in the expression for $Q_{tm}^{\dagger}$ was evaluated numerically, typically by using a Romberg integration scheme. As a check, some numerical integrations were redone with a highly converged Monte Carlo scheme. (Both methods are options in the VariFlex program package used for all calculations.) The comparison of results of both integration methods confirms that the integration parameters for the Romberg method guarantee convergence of the rate constant to better than 1%.

Although formally, the minimization in this example occurs in a four dimensional space, the presence of a symmetry plane in CFH_2 requires that the optimal pivot point be located in that plane. This can only occur if the optimal value of β is either 0 or π. As a check on the minimization procedure, in Figure 3 the computed rate constant at 600 K at a fixed value of R and d is displayed for optimal values of α and discrete values of β. (As will be described later, the fixed values of R and d are in fact optimal values at 600 K.) Clearly, the overall minimum in the rate constant occurs when $\beta = 0$, corresponding, as expected, to the optimal pivot point residing in the symmetry plane.

In addition to properly reflecting symmetry constraints, the results in Figure 3 show that the structure in parameter space about a minimum is quadratic only in a limiting sense. Clearly, the results in the figure show a much more rapid rise in the rate constant on the small α side of the minimum. This is also a typical situation for minimization in R or d. The origin of this behavior is that the hindrance potential occurs in an exponential in the integrand [see eq 24]. Relatively small variations in the RC value or definition cause the hindered rotations to experience relatively small variations in the hindrance potential which then get amplified in the exponential. Even in close proximity to the minimum the nonquadratic

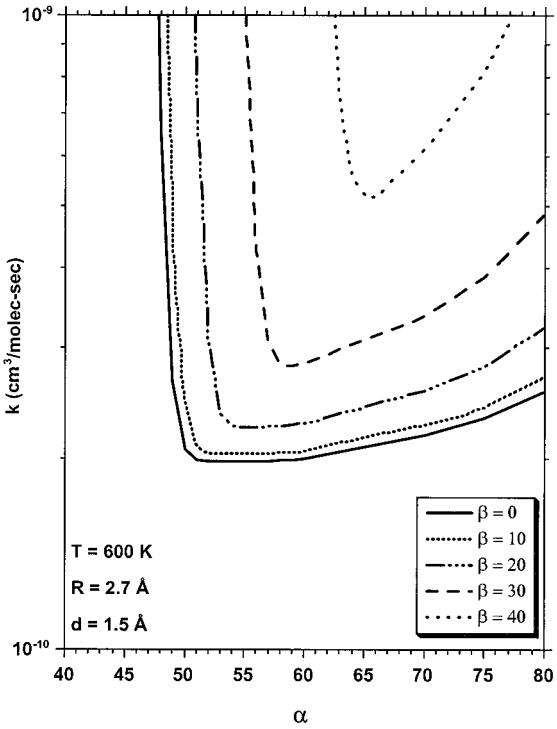

Figure 3. Plot of the calculated canonical rate constants at 600 K versus a for a series of β values with R and d fixed. The minimum in the lowest curve, namely that for $\beta = 0°$, gives the optimum rate constant for the given R and d.

behavior of the parameter surface can make the minimum difficult to locate, especially when the global minimum is one of many local minima. This situation places a premium on a computationally efficient implementation of FTST-VRC, as is offered in the paper. It also supports the use of canonical rate constant approaches to locating minima and then more accurately exploring their vicinity in parameter space in subsequent, more computationally intensive microcanonical studies.

As has already been suggested, minimization in the four parameter space of this example produces local minima. In fact, three distinct, physically intrepretable local minima do occur, all with pivot points in the symmetry plane. This is illustrated in Figure 4 where the computed rate constant at 600 K, minimized with respect to R and α, is plotted versus d for the two possible values of β: "d"< 0 in the figure implies $\beta = \pi$ while "d"> 0 implies that $\beta = 0$. Three minima are clearly seen and indicated by symbols in the figure. They are also labeled "frontside", "bothside", and "backside". The intent of these labels is most conveniently understood in terms of a picture of CFH_2 superimposed on the principal axis system which defines α and β. That is found in each of the four panels of Figure 5, a complicated figure which will be fully described shortly. Each panel shows the z axis from which α is measured as nearly the C−F bond axis, whereas the x axis from which β is measured defines, along with the z axis, the symmetry plane of CFH_2. (Only one H atom is displayed in each panel of Figure 5 because the second H atom lies directly below the first on the other side of the symmetry plane.) Each panel of Figure 5 displays a dotted line representing the equal splay axis which lies in the symmetry plane.

By reference to Figure 5, a positive value of d, corresponding to $\beta = 0$, lies on the $+x$ side of the symmetry plane. Any pivot point on this side would have a projection on the equal splay axis that points in a direction opposite from that of the F and H atoms. We call this the "front" side of the equal splay axis where

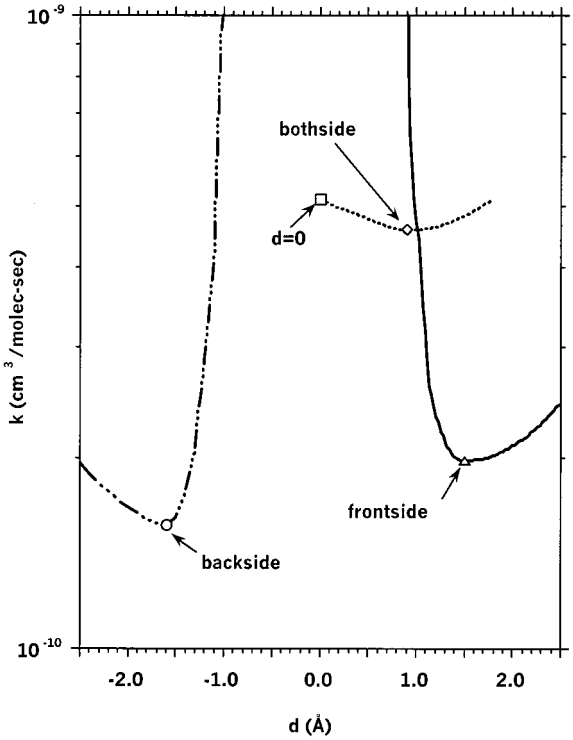

Figure 4. Calculated canonical rate constant versus the length *d* of the pivot point displacement vector **d** at 600 K. The rate constants from which the curves are constructed are optimized (minimized) with respect to 2-dimensional variations in the separation R between the H atom and the tip of **d** and variations in the spherical angle α between *d* and the principal *z*-axis. Negative values of *d* signify that the azimuthal angle β for the vector *d* is 180°. Positive values of *d* signify $\beta = 0°$. The symbols indicate the location of local minimum, except for the open square which locates the lowest rate if $d = 0$ and there is no optimization of the reaction coordinate. See text for meaning of the labels of each local minimum.

the radical p-orbital on the carbon is the most exposed. On the other hand, a negative value of *d* corresponding to $\beta = \pi$ lies on the -*x* side of the symmetry plane with a pivot point projection on the equal splay axis that points in a direction similar to that of the F and H atoms. We call this the "back" side of the equal splay axis where the radical p-orbital on the carbon is most sterically hindered. In Figure 4, large positive (negative) values of *d* have pivot points located in front (back) of the splayed CFH_2. Small values of *d* refer to pivot points for which the transition state samples both the front and backside of the radical orbital and thus are labeled as "bothside". In Figure 4, there is an open square labeled "$d = 0$". This corresponds to a rate constant calculation in which no pivot point optimization occurs and the pivot is thus the center of mass of CFH_2. As the figure indicates this is not a local minimum with respect to variation in *d* but is instead the end of a variation about the "bothside" local minimum located at a relatively small value of *d*.

Although Figure 4 clearly displays three minima and indicates what half of the symmetry plane the minima lie on, it does not indicate the optimal values of *R* and α for each minima. That is displayed in the last three panels of Figure 5, whereas the first panel illustrates the $d = 0$ case for comparison. Each circle drawn on each panel has a radius that corresponds to the optimal value of *R* and a center that locates the optimal pivot point and thus the optimal values of α and *d*. Although Figure 4 was only for 600 K, each panel in Figure 5 shows the optimal pivot point location and *R* value for 300, 600, and 2000 K. Finally, in each of the last three panels of Figure 5, the optimal *d* vectors corresponding to 300 K (longer vector) and 2000 K (shorter vector) are drawn in as thin solid arrows. (The third **d** vector associated with 600 K was not drawn since it is almost identical to that associated with 2000 K, as is reflected in the near concentricity of the 600 and 2000 K circles.) In configuration space, the canonical transition state dividing surface for the nonlinear top + atom combination is a sphere of radius *R* centered on the tip of the associated **d**. The projection of this dividing surface on the $x - z$ plane is a circle. Thus in each panel, it is easy to imagine the spherical dividing surface 300, 600, and 2000 K from the circles in the figure. The transition state species CFH_2...H undergoes large amplitude, 2-dimensional hindered motion on the surface of this spherical dividing surface. The more conventional picture of the dividing surface being a harmonic oscillator type motion in a plane perpendicular to the reaction path still applies to the conserved degrees of freedom. But the FTST ansatz has replaced that picture for transitional modes with a curvelinear coordinate representation leading to the spherical transition state dividing surfaces found in Figure 5.

Panel (a) in Figure 5 displays the resulting optimal values of $R = R_{cm}$ in this case. Clearly, the circles for the three different temperatures are centered on the center of mass which is at the origin of the $x - z$ plane. In the figure, the radius of a circle decreases as its corresponding temperature increases. This is just a representation of the well-known fact that for barrierless reactions the transition state moves in along the reaction path as the temperature increases. If one were to employ a conventional planar transition state dividing surface perpendicular to a reaction path, there would be in this example two transition states corresponding to two different reaction paths—one for forward attack approximately along the equal splay axis in the $x > 0$ portion of the $x - z$ plane and one for backward attack approximately along the same axis in the $x < 0$ portion of the plane. Two separate calculations would be performed and the results summed. (This raises a series of chemical issues regarding the role of the CFH_2 umbrella motion; a limited discussion is provided at the end of this section.) In this anharmonic approach, the same dividing surface spans both reaction paths. Reactant flux can enter from both the front and the back and the formalism discussed in the previous sections takes all of this into proper account. However, the circles in the figure do not intersect the equal splay axis at right angles because the equal splay axis is centered on the C atom and not on the center of mass. This means that even if we replaced the actual hindering potential on the sphere by a harmonic version originating from a point where the equal splay axis intersects the sphere, the harmonic frequencies associated with that potential might not closely approximate the harmonic frequencies perpendicular to the equal splay axis. Does this make the constrained $d = 0$ result inaccurate?

The answer to that question can be determined by simply letting the pivot point location vary from $d = 0$ to see if the rate constant can be further minimized. That is exactly what the solid line labeled "bothside" in Figure 4 represents for $T =$ 600 K. Note that starting from $d = 0$, the minimum with respect to *R* and α could have gone into the $\beta = 0$ or π region. As the figure indicates, the minimum goes only to the $\beta = 0$ region. In other words, for small nonzero d, any attempt to locate the pivot point in the $x < 0$ portion of the $x - z$ plane produces a rate constant higher than values for the same *d* in $x > 0$ portion of the plane. The resulting minimum in this optimization starting from $d = 0$ is indicated with an open diamond and the label "bothside" in Figure 4. The corresponding transition state

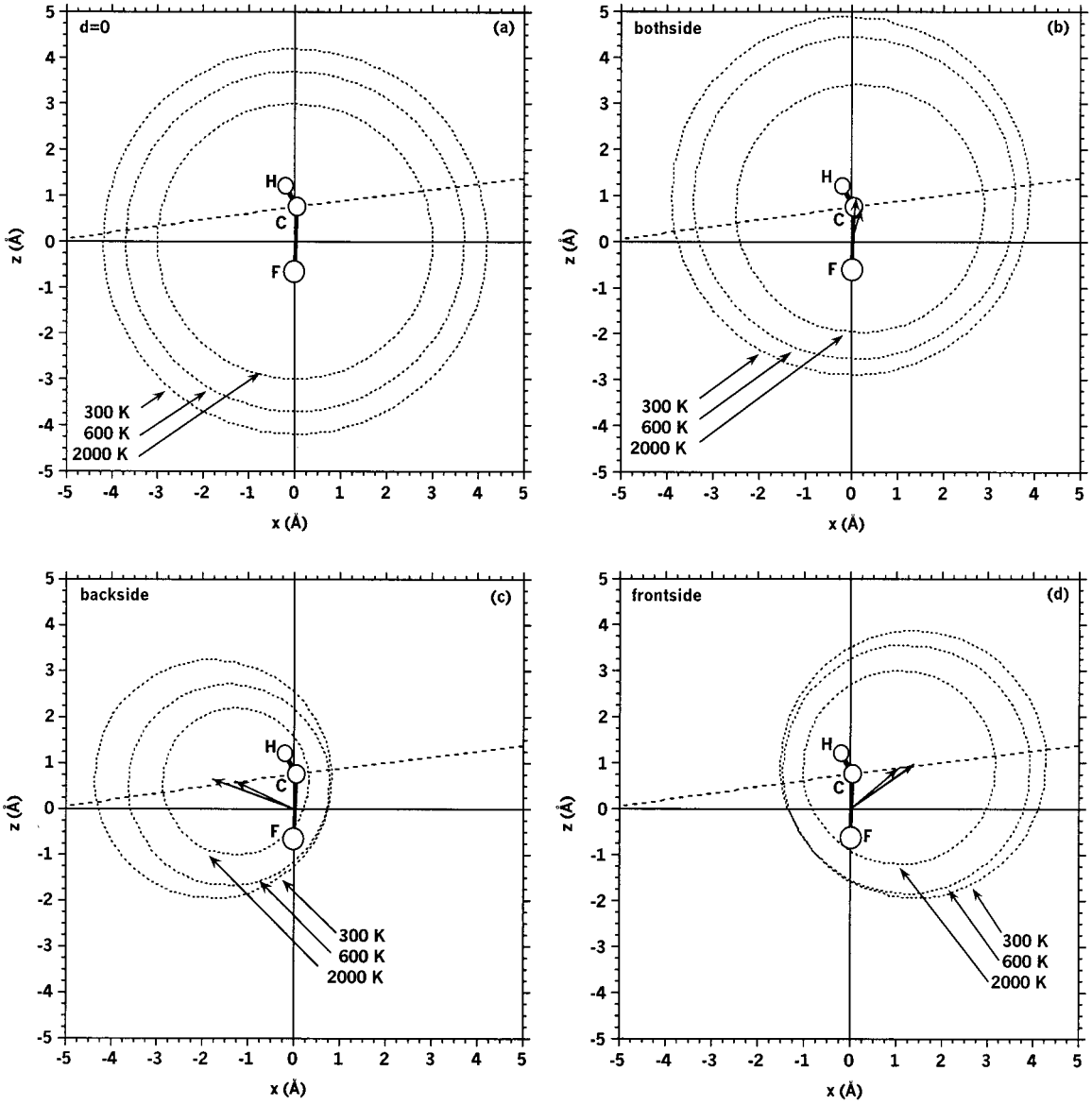

Figure 5. Depiction of the transition state dividing surfaces at 300, 600, and 2000 K for the (a) $d = 0$, (b) bothside, (c) backside, and (d) frontside cases discussed in the text and presented in Figure 4. In this two-dimensional representation in the $x-z$ plane, each dividing surface is a circle centered on the pivot point at the tip of the **d** vector. The latter appears as a thin solid arrowed line emanating from the origin and varies in length (d) and orientation (α) with temperature. The origin is at the center of mass of CFH_2 which lies approximately on the C−F bond. In panel (a), $d = 0$ and the circles are centered on the origin. In panels (b)−(d), only the **d** vectors corresponding to 300 K (longer vector) and 2000 K (shorter vector) are shown. (The third **d** vector associated with 600 K was not drawn since it is almost identical to that associated with 2000 K, as is reflected in the near concentricity of the 600 and 2000 K circles.) The dashed line in each panel is the equal splay axis defined in the text.

dividing surface for 600 K and also for 300 and 2000 K are indicated in panel (b) of Figure 5. Unlike panel (a), one **d** vector can be seen in the panel (it is for 2000 K), whereas the other two **d** vectors are largely hidden by the representation of the C−F bond in the panel. The relative positions of the circles indicate that the optimum pivot point has moved up the C−F bond to reside very close to the C atom as temperature increases. As a result the transition state dividing surfaces intersect the equal splay axis minimum energy path closer to right angles than in panel (a) and this tendency increases with temperature. The change of pivot point location from panel (a) to panel (b) is consistent with the observations of Klippenstein[7,9] in other recombination reactions to which he has applied both bond coordinate and center-of-mass coordinate reaction coordinate descriptions and so identified so-called inner and outer transition states, respectively. As Klippenstein has discovered in a number of reactions, optimization of the pivot point tends to localize the pivot on the radical atom at higher temperatures while at lower temperatures, the larger radius of the transition state location tends to favor a center of mass location. The optimization in R, d, and α involved stepping through distances in 0.1 Å increments and angles in 5° increments. Thus there is some imprecision in transition state parameters but Figure 4 indicates that the kinetic consequence of variations in step sizes is not important once you are near the minimum and the step sizes are small enough. The variation of the rate constant between the dividing surfaces of panel (a) and panel (b) is less than 10%. The "bothside" label of the minimum just emphasizes that, for this transition state dividing surface, significant flux enters from both the front and back approach of the H in its attack on CFH_2.

The open triangle at the minimum of the dotted curve in Figure 4 specifies a "frontside" transition state (at 600 K) whose dividing surface, along with that for 300 K and 2000 K, are indicated in panel (d) of Figure 5. The analogous "backside"

transition state is indicated by the open circle at the minimum of the dot−dash curve in Figure 4 and by dividing surfaces for all three temperatures in panel (c) of Figure 5. In Figure 5, it is clear that for both the backside or frontside cases the transition state dividing surface sphere is centered somewhere in the vicinity of the equal splay axis. However, rather than being centered at the atom, it is centered somewhere on the radical orbital (not shown) that points both in front of and in back of the radical carbon atom. It is also clear that although the radius of that sphere shrinks noticeably with temperature, the center of the sphere changes much less so with temperatures, having essentially identical values of d at 600 and 2000 K. The radii of the spheres are smaller than the transition state dividing surfaces of panels (a) and (b) of Figure 5 with the consequence that a portion of each circle is very close to the two H atoms and the F atom on the CFH_2 radical. In the vicinity of these three atoms, the PES on these dividing surfaces is generally highly repulsive resulting in almost no flux entering the dividing surface in these regions. This is the motivation for the labels "frontside" and "backside". The frontside transition state has almost no reactive flux entering from the backside reaction path on the $x < 0$ portion of Figure 5. Correspondingly, the backside transition state has almost no reactive flux entering from the frontside reaction path on the $x > 0$ portion of Figure 5. In this sense, the two transition states are uncoupled, just as they would be in the usual harmonic oscillator treatment of a separate planar dividing surface for each reaction path. As shown in Figure 4, the kinetic consequences of this "specialization" of the transition state to each of the two reaction paths is very significant. Much of this significance is due to the fact that confining a rate coefficient calculation to only one of two reaction paths approximately halves the rate. However, as Figure 4 indicates, the frontside and backside rates are each less than half as small as the bothside rate.

There are three aspects of Figure 4 that require further discussion. First, the large variation in the rate constant as d becomes small for both the frontside and backside cases in Figure 4 are in contrast to the much more gentle variation in the bothside case. The close approach of the frontside or backside transition state dividing surface to the atoms in the CFH_2 fragment means that a large portion of that dividing surface is in a region of rapidly varying potentials, both the largely repulsive nonbonding interactions and the deeply attractive or steeply repulsive Morse oscillator attractive potential (see eq 21). Because potentials appear in an exponential argument in CFTST, it is not surprising that relatively minor variations in d can cause large variations in the rate constant. In contrast, the bothside cases, as shown in panels (a) and (b) of Figure 5, do not involve such close approaches and largely sample regions where the potential varies much more gradually. This gives rise to a more gradual variation in the rate constant in $R - \alpha$ space. Large variations in the computed rate constant were previously discussed for Figure 3 and were explained in a similar manner. The results in that figure represent variations about the minimum in the frontside approach at 600 K found in Figure 4 and Figure 5.

The second aspect of Figure 4 concerns the bothside case. As d tends toward larger values, the curvature about the local minima in $R - \alpha$ space flattens out until, at large enough values of d, there is no longer a minimum. Thus the variation in Figure 4 has distinct end points − terminating at $d = 0$ because $\beta = 0$ is always perfered and terminating at some relatively small positive value of d when there is no longer a minimum. The loss of a minimum is also true for the frontside and backside

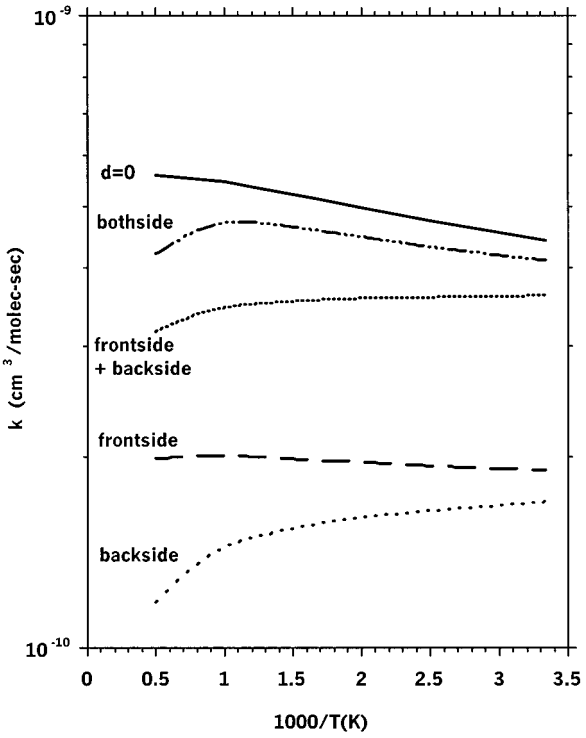

Figure 6. Calculated canonical rate constant versus inverse temperature for $d = 0$ (solid line), bothside (dash−dot), frontside + backside (dot), frontside (long dash), and backside (short dashes) cases. The frontside + backside curve is simply the sum of the backside curve and the frontside curve. See text for details.

local cases as d approaches zero, although when this occurs the rate is so large that it is off scale in the figure. This kind of behavior is typical in systematic and detailed optimization of the RC definition and places a premium on efficient evaluation of FTST-VRC reaction rate constants in order to rapidly survey large regions of parameter space.

The third and last aspect of Figure 4 concerns both frontside and backside cases. In these two cases, the difference between the optimal value of R and the given value of d decreases as the absolute value of d increases. In fact, for the extreme ends of Figure 4, $|d|$ exceeds the optimal value of R. As discussed in the previous section, this corresponds to a case where not all of the full angular range of the internal angles (θ_1, ϕ_1) is required to specify all possible relative orientations of H with respect to CFH_2. The smooth behavior of all the curves in Figure 4 indicates that the onset of this limitation produces no irregularity in the minimization procedure. As it happens, at all temperatures investigated for this reaction, the optimal dividing surface corresponds $|d| < R$.

In Figure 6, the computed canonical rate constants are displayed as a function of temperature for the three different dividing surfaces as labeled as in Figures 4 and 5. The diamond, triangle, and circle minima displayed in Figure 4 are the 600 K values in Figure 6 of the rate constants labeled bothside, frontside, and backside, respectively. For comparison the rate constant when d is constrained to be 0 is also displayed in Figure 6 and its 600 K value is the open square in Figure 4. The rate constant curve labeled "frontside + backside" is, as the name implies, the sum of the frontside and backside rate constants. This is the kinetic consequence of the previous interpretation of the frontside and backside dividing surfaces each heavily favoring one of two reaction reaction paths available for the H + CFH_2 reaction.

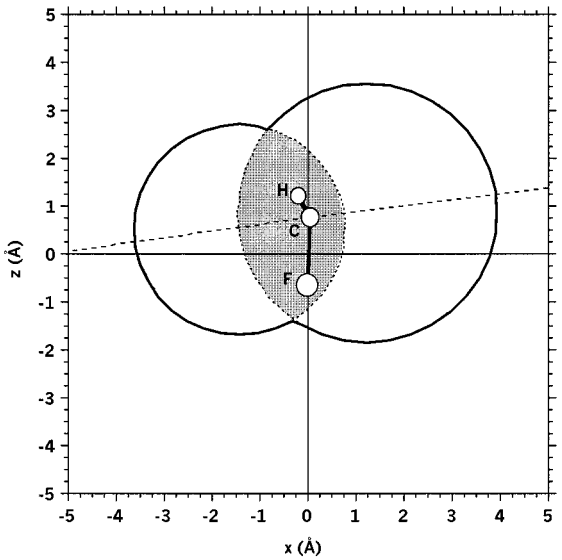

Figure 7. Transition state dividing surface at 600 K formed from the combination of the backside dividing surface of Figure 5c and the frontside dividing surface of Figure 5d. Shaded region is the overlap of frontside and backside dividing surface. Other features of the plot are as in Figure 5.

The results in Figure 6 show that exploring reaction coordinates that are only mildly different from a CMRC (by searching parameter space with small values of d beginning at $d = 0$) lowers the rate constant by approximately 10% except at the highest temperatures where the reduction approaches 25%. This changes a uniformly increasing rate with temperature into a mildly decreasing rate at high temperatures. The sum of the frontside and backside rates involves a further reduction from the bothside value of between about 10% at low temperatures to 25% at high temperatures. This further changes the temperature dependence to one that is uniformly decreasing.

Since the typical kinetics measurement of the reaction rate for $H + CFH_2$ would not distinguish whether addition occurred via a front or back approach, neither the frontside or the backside computed rate constant in Figure 6 is appropriate for comparison to experiment. Because the variational principle of kinetics is based on the fact that statistical theories always approach the true rate constant from above, the computed rate constant constrained by $d = 0$ in Figure 6 cannot be the best theoretical estimate because it is higher than other statistical calculations. This leaves two remaining computed rate constants in Figure 6 labeled "bothside" or "frontside + backside". Of these two, the best theoretical estimate can be selected by application of the variational principle in the following manner.

From Figure 5c and 5d, the frontside and backside dividing surfaces intersect to form a combined exterior surface that is something like a snowman lying on its side. Its projection on the symmetry plane is shown as the heavy outline in Figure 7 for the combination of the optimal frontside and backside dividing surfaces at 600 K. For convenience, we will call this dividing surface the "snowman" dividing surface. In principle FTST-VRC theory based on such a dividing surface could be formulated in the same manner as has been done in this paper for a spherical dividing surface. However, the kinetic energy operator as embodied in $\mathbf{A_r}$ would have to be known for snowman surfaces about each reactant, whereas, in fact, the operator has been explicitly developed only for spherical surfaces (regular spherical surface for a nonlinear top + atom). Nonetheless, suppose a snowman FTST-VRC theory had been formulated. Its application to the specific dividing surface in Figure 7 would produce a rate constant that is independent of the nature of the potential energy in the interior of the surface because statistical theories for recombination are only sensitive to the potential energy on the dividing surface itself (see eq 25). In particular, the snowman FTST-VRC would be insensitive to a potential energy surface that was infinitely repulsive in the interior shade region of Figure 7. However, for such a potential energy surface, the sum of the separately calculated frontside and backside FTST-VRC rate constants would be rigorously identical to the snowman FTST-VRC rate constant. This is due to the fact that the portion of either the frontside or backside dividing surface with an infinitely repulsive potential would rigorously receive zero reactive flux. As a consequence, the reactive flux that did enter either the frontside or the backside dividing surface would be exactly identical to that entering the snowman dividing surface.

In fact, any realistic potential energy surface will not be infinitely repulsive in the shaded region of Figure 7. Therefore the sum of the frontside and backside FTST-VRC rate constant are not equal to the snowman FTST-VRC rate constant. However, a realistic representation of the potential energy surface in the shaded region can only make both the frontside and backside FTST-VRC rate constants larger than they would have been with an infinitely repulsive potential. Consequently, the sum of the frontside and backside FTST-VRC rate constants is always a rigorous upper bound to the snowman FTST-VRC rate constant. This is a completely generic statement about any combination of rate constants for separately calculated spherical dividing surfaces. Of the three distinct dividing surfaces mentioned in this application, namely frontside, backside, and bothside, the sum of any pair of separately optimized rate constants or the triple sum of all three separately optimized rate constants is an upper bound to an FTST-VRC rate constant for a dividing surface of the corresponding, more complex nonspherical exterior shape. That combination or that individual rate constant that gives the lowest FTST-VRC rate constant while simultaneously sampling all the relevant reaction pathways is by the variational principle the best estimate of the rate constant. From Figure 6, the best estimate of the rate constant is therefore the curve labeled "frontside + backside".

As is indicated in Figure 5, either the frontside or backside dividing surfaces have pivot points unconnected to atom or bond locations. In fact the pivot points are located somewhere in the center of the lobes of the radical p-orbital. This kind of behavior is not unusual. Klippenstein and Harding have suggested[4] that such pivot points allow the dividing surface to more perfectly follow the contours of the radical orbitals on isolated reactants. This particular application is consistent with such a view.

Although the above analysis correctly selects, for this model of the $H + CFH_2$ reaction, a combination of frontside and backside dividing surfaces, the prominence of these two surfaces raises chemical issues about the umbrella motion of the CFH_2 radical. This motion could flip the radical back and forth between a "front" and "back" posture with respect to the attacking H atom. These chemical issues are important but not directly relevant to this paper which is using $H + CFH_2$ only as an example of the features and implications of the formalism developed. However, CFH_2 is splayed in its equilibrium conformation and the inversion barrier from ab initio calculations[19] is substantial at about 9 kcal/mol. The more fluorine is substituted for hydrogen in CFH_2, the larger this inversion barrier becomes. After the transition state dividing surface is crossed, a H−C bond is formed and for some CFxHy radicals, CFH_2 being one, the kinetic energy released by the formation of that bond is more than enough to surmount any inversion

barrier. Thus although the front and backside reaction paths are different, the product molecule CH_3F is the same. Thus it is certainly fair to say that splayed molecules with a forward and backward reaction path do exist and the example given in this paper is not unrealistic. However, the details of the PES are important in the chemical accuracy of each application and the results presented here do not attempt to attain that accuracy.

4. Discussion and Summary

In this paper, an explicit general rate constant expression of flexible transition state theory with variable reaction coordinate has been developed. This expression implements theory derived elsewhere by constructing explicit formulas for the kinetic energy of external rotational and transitional hindered rotational degrees of freedom executing motion about the collision center of mass (external rotations) or fixed reactant-based pivot points (hindered rotations). With these formulas, the flexible transition state theory expression for either the canonical or microcanonical rate constant can be written as an explicit function of pivot point location on each reactant and the separation between the pivot point on each reactant. The minimization of the rate constant with respect to pivot point location is equivalent to optimizing the reaction coordinate definition, whereas minimization with respect to the separation locates the most constrictive reaction bottleneck along the optimal reaction coordinate. The expressions developed apply to all five combinations of reactant top types in bimolecular collisions: linear-top + atom, nonlinear-top + atom, linear-top + linear-top, nonlinear-top + linear-top, and nonlinear-top + nonlinear-top. The expression are analytic except for a hindering function which involves a numerical integration over the internal angles (from one to five depending on the case). The integrands in the integration are all analytic, though tedious for the most complicated cases. The formulas developed here have already been coded and implemented in the freeware package VariFlex,[14] which was used for all the calculations contained in this paper.

The applications of the expressions are illustrated at only the canonical level for a model potential qualitatively related to $CFH_2 + H$. The effect of optimizing the reaction coordinate on the canonical rate constant is a reduction by a factor of between 20% to 45% depending on the temperature. A reduction is the expected result in the context of a variational theory. The reduction factor exceeds the anticipated error inherent in using a canonical treatment instead of the (correct) microcanonical treatment. This error is estimated to be 10−20% based on detailed studies of the benchmark $CH_3 + H$ and $CH_3 + CH_3$ recombination reactions.[20,21] Application of our microcanonical treatment for variable reaction coordinate to several prototype reactions and comparison to the corresponding canonical rate coefficients has yet to be undertaken but will form part of a future paublication. For the CFH_2 fragment, which is an asymmetric top, these reaction coordinate optimizations result in pivot points which do not lie at the center-of-mass of CFH_2 nor at the 'radical' atom (carbon), nor along the C−F or C−H bonds, but within the radical p-orbital extending in front of and behind the carbon atom. Furthermore, the lowest and therefore best rate constant is achieved by the sum of separate rate constant calculations for optimal reaction coordinates specialized to H atom attack on either the front or the back of the radical p-orbital on carbon. Optimized reaction coordinates that equally sample front and back attack are only a local, not global, minimum in the computed rate constant. The presence of multiple minima in the rate constant minimization process emphasizes the value of compact, computationally efficient expressions which this paper is attempting to provide.

The formal development presented goes to the limit of what can be done to optimize the transition state dividing surface within the ansatz of a single pivot point on each reactant about which to execute hindered rotations. Such an ansatz produces spherical dividing surfaces for which only the radius can be optimized. The explicit expressions here do that and the application to the $CFH_2 + H$ reaction clearly illustrates the spherical nature of the optimal dividing surfaces. However, hindered rotations in chemical reactions can execute coordinated motion about multiple pivot points, giving rise to more flexible dividing surfaces much more complicated than spheres. For the nonlinear or linear top cases, the simplest example of this is an elliptical dividing surface whose two foci are, in effect, two pivot points on the nonatom reactant. The more flexible the dividing surface the larger the parameter space within which the reaction coordinate can be optimized. That optimization lowers the rate constant and, by the variational principle for statistical theories, the lower the computed rate constant the more accurately it estimates the actual rate constant. Further developments in flexible transition state theory can proceed in this direction.

However, as the application illustrated, the formalism developed here can be used in principle to estimate the rate constant for an arbitrary dividing surface. Any dividing surface can be approximated by impregnating the surface with a uniform coating of small spheres intersecting so that there are no "holes" in the dividing surface. If the radii of the spheres are reduced but the number of spheres are increased to maintain a uniform coating of intersecting spheres, the coating approximates to finer and finer detail every feature of the dividing surface. The formalism developed here allows the treatment of each individual sphere. However, as in the application, flux entering the face of each sphere pointing into, rather than out from, the dividing surface must be negated. As in the application, that can be conceptually achieved by positing an infinitely repulsive potential in the overlap region of the sphere and the dividing surface it is impregnating. In actuality, the negation would be achieved by limiting the range of the integration variables in the multidimensional integral required by the theory (see eq 24). Each resulting rate constant calculated separately for each sphere can then be summed to get an estimate for the desired rate constant that becomes more and more exact as the radius of the touching spheres in the coating is decreased.

The developments of this paper streamline the treatment of any bimolecular reaction within the context of canonical or microcanonical flexible transition state theory with variable reaction coordinates. The only limitation to an application is that of reliable interaction potentials in the kinetically interesting region. Because of advances in electronic structure theory and the associated computer codes, and the existence of faster computers with larger memory, these potentials are become increasingly available. Application of this theory to *a variety of* recombination reactions will be included in subsequent papers. A detailed comparison of our approach with other transition-state or collision-theory based treatments of rates (e.g., work of S. J. Kleippenstein, S. Smith, R. Levine, R. A. Marcus) will be the subject of a separate publication.

Acknowledgment. A. F. W. was supported by the U.S. Department of Energy, Office of Basic Energy Science, Division of Chemical Sciences, under contract No. W-31-109-ENG-38. D.M.W.was supported by a research grant from the Natural Sciences and Engineering Research Council of Canada.

Appendix

A. Kinetic Energy Tensors for Center-of-Mass Reaction Coordinate. Analytic expressions for $\mathbf{A}_r^0$, $|\mathbf{A}_r^0|$, and the required elements of $\mathbf{G}_r^0$ are listed below in subsections A.1−A.5 for the five combinations of top types. (Atom + atom combination is excluded; the matrix elements $(G_r^0)_{ij}$, $i, j = 1, 2, 3$ are not required.) These expressions are functions of the internal angles $\mathbf{q}_{cm,int}$, of the moments of inertia of the fragment tops, and of the 'external' moment of inertia $\mathbf{I}_{ex} = \mu R_{cm}^2$ for the mutual rotation of the centers-of-mass of fragments 1 and 2 about the overall center-of-mass. The abbreviations $C_\theta = \cos\theta$, $S_\theta = \sin\theta$, $C_\phi = \cos\phi$, etc. are used throughout.

The dimension of the reduced matrixes $\mathbf{A}_r^0$ and G_r^0 is $n \times n$; both matrixes are symmetric. The full $(n + 1) \times (n + 1)$-dimensional matrixes $\mathbf{A}^0$ and $\mathbf{G}^0$ differ from $\mathbf{A}_r^0$ and $\mathbf{G}_r^0$ by the addition of a $(n + 1)^{st}$ row and $(n + 1)^{st}$ column. Each additional matrix element is 0 except for $(\mathbf{A}^0)_{n+1,n+1} = \mu$ and $(\mathbf{G}^0)_{n+1,n+1} = \mu^{-1}$. In terms of $\mathbf{A}_r^0$, the 'reduced' kinetic energy which results from subjecting the 'full' kinetic energy expression to the constraint $\dot{R}_{cm} = 0$ (see Section III of Paper III) is

$$2T^{0*} = \dot{\mathbf{Q}}_{cm,r}^T \cdot \mathbf{A}_r^0 \cdot \dot{\mathbf{Q}}_{cm,r}$$

where $\dot{\mathbf{Q}}_{cm,r}^T = (\omega_x, \omega_y, \omega_z, \dot{\mathbf{q}}_{cm,int})$ is the reduced generalized velocity vector corresponding to $\dot{\mathbf{Q}}_{cm}^T$ which is defined immediately below eq 11).

A.1 Linear Top-Atom ($n = 4$). Moment of inertia − Fragment 1: $I = I_1$

$$\dot{\mathbf{Q}}_{cm,r}^T = (\omega_x, \omega_y, \omega_z, \dot{\theta} = \dot{\theta}_1)$$

$$A_r^0 = \begin{bmatrix} I\cos^2\theta + I_{ex} & 0 & I\cos\theta\sin\theta & 0 \\ 0 & I + I_{ex} & 0 & -I \\ I\cos\theta\sin\theta & 0 & I\sin^2\theta & 0 \\ 0 & -I & 0 & I \end{bmatrix}$$

$$|\mathbf{A}_r^0| = \sin^2\theta\, I_{ex}^2\, I^2$$

Inverse elements

$$(G_r^0)_{44} = \frac{I + I_{ex}}{I\, I_{ex}}$$

A.2 Nonlinear Top-Atom ($n = 5$). Moments of inertia − Fragment 1: $I_a = I_{1a}$, $I_b = I_{1b}$, $I_c = I_{1c}$

$$\dot{\mathbf{Q}}_{cm,r}^T = (\omega_x, \omega_y, \omega_z, \dot{\theta} = \dot{\theta}_1, \dot{\phi} = \dot{\phi}_1)$$

$$\mathbf{A}_r^0 = \begin{bmatrix} I_{xx} & \Delta_C & I_{xz} & -I_a S_\theta & \Delta_C \\ \Delta_C & I_{yy} & \Delta_S & 0 & I_c Sf^2 + I_b C_\phi^2 \\ I_{xz} & \Delta_S & I_{zz} & I_a C_\theta & \Delta_S \\ -I_a S_\theta & 0 & I_a C\theta & I_a & 0 \\ \Delta_C & I_c Sf^2 + I_b C_\phi^2 & \Delta_S & 0 & I_c Sf^2 + I_b C_\phi^2 \end{bmatrix}$$

where

$$\Delta_C = (I_c - I_b) C_\theta C_\phi S_\phi$$

$$\Delta_S = (I_c - I_b) S_\theta C_\phi S_\phi$$

$$I_{xx} = (I_c C_\phi^2 + I_b S_\phi^2) C_\theta^2 + I_a S_\theta^2 + I_{ex}$$

$$I_{xz} = (I_c C_\phi^2 + I_b S_\phi^2 - I_a) S_\theta C_\theta$$

$$I_{yy} = I_c S_\phi^2 + I_b C_\phi^2 + I_{ex}$$

$$I_{zz} = (I_c C_\phi^2 + I_b S_\phi^2) S_\theta^2 + I_a C_\theta^2$$

Inverse elements

$$(G_r^0)_{44} = \frac{1}{I_{ex} S_\theta^2} + \frac{1}{I_a} + \frac{C_\theta^2}{S_\theta^2}\left(\frac{S_\phi^2}{I_b} + \frac{C_\phi^2}{I_c}\right)$$

$$(G_r^0)_{45} = \frac{\Delta_C}{I_b I_c S_\theta}$$

$$(G_r^0)_{55} = \frac{1}{I_{ex}} + \frac{C_\phi^2}{I_b} + \frac{S_\phi^2}{I_c}$$

A.3 Linear Top-Linear Top ($n = 6$). Moments of inertia − Fragment 1: I_1 Fragment 2: I_2

$$\dot{\mathbf{Q}}_{cm,r}^T = (\omega_x, \omega_y, \omega_z, \dot{\theta}_1, \dot{\theta}_2, \dot{\chi})$$

$$\mathbf{A}_r^0 = \begin{bmatrix} I_{xx} & I_{xy} & I_{xz} & 0 & I_2 S_\chi & I_2 S_{\theta 2} C_{\theta 2} C_\chi \\ I_{xy} & I_{yy} & I_{yz} & -I_1 & -I_2 C_\chi & I_2 S_{\theta 2} C_{\theta 2} S_\chi \\ I_{xz} & I_{yz} & I_{zz} & 0 & 0 & I_2 S_{\theta 2}^2 \\ 0 & -I_1 & 0 & I_1 & 0 & 0 \\ I_2 S_\chi & -I_2 C_\chi & 0 & 0 & I_2 & 0 \\ I_2 S_{\theta 2} C_{\theta 2} C_\chi & I_2 S_{\theta 2} C_{\theta 2} S_\chi & I_2 S_{\theta 2}^2 & 0 & 0 & I_2 S_{\theta 2}^2 \end{bmatrix}$$

$$|\mathbf{A}_r^0| = S_{\theta 1}^2\, S_{\theta 2}^2\, I_{ex}^2\, I_1^2\, I_2^2$$

where

$$I_{xx} = I_2 S_\chi^2 + I_2 C_\chi^2 C_{\theta 2}^2 + I_1 C_{\theta 1}^2 + I_{ex}$$

$$I_{xy} = -I_2 S_\chi C_\chi S_{\theta 2}^2$$

$$I_{xz} = I_1 S_{\theta 1} C_{\theta 1} + I_2 S_{\theta 2} C_{\theta 2} C_\chi$$

$$I_{yy} = I_1 + I_2 C_\chi^2 S_{\theta 2}^2 + I_2 C_{\theta 2}^2 + I_{ex}$$

$$I_{yz} = I_2 S_\chi S_{\theta 2} C_{\theta 2}$$

$$I_{zz} = I_1 S_{\theta 1}^2 + I_2 S_{\theta 2}^2$$

Inverse elements

$$(G_r^{\,0})_{44} = \frac{I_1 + I_{ex}}{I_{ex} I_1}$$

$$(G_r^{\,0})_{45} = \frac{C_\chi}{I_{ex}}$$

$$(G_r^{\,0})_{46} = \frac{-C_{\theta 2} S_\chi}{I_{ex} S_{\theta 2}}$$

$$(G_r^{\,0})_{55} = \frac{I_2 + I_{ex}}{I_{ex} I_2}$$

$$(G_r^{\,0})_{56} = \frac{-C_{\theta 1} S_\chi}{I_{ex} S_{\theta 1}}$$

$$(G_r^{\,0})_{66} = \frac{1}{I_1 S_{\theta 1}^{\,2}} + \frac{1}{I_2 S_{\theta 2}^{\,2}} + \frac{1 - \cos 2\theta_1 \cos 2\theta_2 + \sin 2\theta_1 \sin 2\theta_2 C_\chi}{2 I_{ex} S_{\theta 1}^{\,2} S_{\theta 2}^{\,2}}$$

A.4 Nonlinear Top-Linear Top ($n = 7$). Moments of inertia − Fragment 1: I_{1a}, I_{1b}, I_{1c} Fragment 2: I_2

$$\dot{\mathbf{Q}}_{cm,r}^{\,T} = (\omega_x, \omega_y, \omega_z, \dot{\theta}_1, \dot{\phi}_1, \dot{\theta}_2, \dot{\chi})$$

$$\mathbf{A}_r^{\,0} = \begin{bmatrix} I_{xx} & I_{xy} & I_{xz} & -I_{1a} S_{\theta 1} & \Delta_{C1} & -I_{2b} S_\chi & I_2 C_{\theta 2} S_{\theta 2} C_\chi \\ I_{xy} & I_{yy} & I_{yz} & 0 & \Sigma & I_2 C_\chi & I_2 C_{\theta 2} S_{\theta 2} S_\chi \\ I_{xz} & I_{yz} & I_{zz} & I_{1a} C_{\theta 1} & \Delta_{S1} & 0 & I_2 S_{\theta 2}^{\,2} \\ -I_{1a} S_{\theta 1} & 0 & I_{1a} C_{\theta 1} & I_{1a} & 0 & 0 & 0 \\ \Delta_{C1} & \Sigma & \Delta_{S1} & 0 & \Sigma & 0 & 0 \\ -I_2 S_\chi & I_2 C_\chi & 0 & 0 & 0 & I_2 & 0 \\ I_2 C_{\theta 2} S_{\theta 2} C_\chi & I_{2b} C_{\theta 2} S_{\theta 2} S_\chi & I_2 S_{\theta 2}^{\,2} & 0 & 0 & 0 & I_2 \Sigma_{\theta 2}^{\,2} \end{bmatrix}$$

$$|\mathbf{A}_r^0| = S_{\theta 1}^2 S_{\theta 2}^2 I_{ex}^2 I_{1a} I_{1b} I_{1c} I_2^2$$

where

$$\Sigma = I_{1b} C_{\phi 1}^{\,2} + I_{1c} S_{\phi 1}^{\,2}$$

$$\Delta_{Ci} = (I_{ic} - I_{ib}) C_{\theta i} C_{\phi i} S_{\phi i}$$

$$\Delta_{Si} = (I_{ic} - I_{ib}) S_{\theta i} C_{\phi i} S_{\phi i}$$

$$I_{xx} = (I_{1b} + I_{1c} - \Sigma) C^2{}_{\theta 1} + I_{1a} S_{\theta 1}^{\,2} + I_2 C_\chi^{\,2} C_{\theta 2}^{\,2} + I_2 S_\chi^{\,2} + I_{ex}$$

$$I_{xy} = \Delta_{C1} - I_2 C_\chi S_\chi C_{\theta 2}^{\,2}$$

$$I_{xz} = (I_{1b} + I_{1c} - \Sigma - I_{1a}) C_{\theta 1} S_{\theta 1} + I_2 S_{\theta 2} C_{\theta 2} C_\chi$$

$$I_{yy} = \Sigma + I_2 C_\chi^{\,2} S_{\theta 2}^{\,2} + I_2 C_{\theta 2}^{\,2} + I_{ex}$$

$$I_{yz} = \Delta_{S1} + I_2 C_{\theta 2} S_{\theta 2} S_\chi$$

$$I_{zz} = (I_{1b} + I_{1c} - \Sigma) S^2{}_{\theta 1} + I_{1a} C_{\theta 1}^{\,2} - I_2 S_{\theta 2}^{\,2}$$

Inverse elements

$$(G_r^{\,0})_{44} = \frac{1}{I_{ex} S_{\theta 1}^{\,2}} + \frac{1}{I_{1a}} + \frac{C_{\theta 1}^{\,2}}{S_{\theta 1}^{\,2}} \left(\frac{S^2_{\phi 1}}{I_{1b}} + \frac{C^2_{\phi 1}}{I_{1c}} \right)$$

$$(G_r^{\,0})_{45} = \frac{\Delta_{C1}}{I_{1b} I_{1c} S_{\theta 1}}$$

$$(G_r^{\,0})_{46} = \frac{S_\chi}{I_{ex} S_{\theta 1}}$$

$$(G_r^{\,0})_{47} = \frac{C_{\theta 1}}{I_{ex} S_{\theta 1}^{\,2}} + \frac{C_{\theta 1}}{S_{\theta 1}^{\,2}} \left(\frac{S_{\phi 1}^{\,2}}{I_{1b}} + \frac{C_{\phi 1}^{\,2}}{I_{1c}} \right) - \frac{C_{\theta 2} C_\chi}{I_{ex} S_{\theta 1} S_{\theta 2}}$$

$$(G_r^{\,0})_{55} = \frac{S_{\phi 1}^{\,2} I_{1b} + C_{\phi 1}^{\,2} I_{1c}}{I_{1b} I_{1c}} + \frac{1}{I_{ex}}$$

$$(G_r^{\,0})_{56} = \frac{C_\chi}{I_{ex}}$$

$$(G_r^{\,0})_{57} = \frac{C_{\theta 2} S_\chi}{I_{ex} S_{\theta 2}} + \left(\frac{1}{I_{1b}} - \frac{1}{I_{1c}} \right) \frac{C_{\phi 1} S_{\phi 1}}{S_{\theta 1}}$$

$$(G_r^{\,0})_{66} = \frac{I_2 + I_{ex}}{I_2 I_{ex}}$$

$$(G_r^{\,0})_{67} = \frac{C_{\theta 1} S_\chi}{I_{ex} S_{\theta 1}}$$

$$(G_r^{\,0})_{77} = \frac{1}{S_{\theta 1}^{\,2}} \left(\frac{S_{\phi 1}^{\,2}}{I_{1b}} + \frac{C_{\phi 1}^{\,2}}{I_{1c}} \right) + \frac{1}{I_2 S_{\theta 2}^{\,2}} + \frac{1 - \cos 2\theta_1 \cos 2\theta_2 + \sin 2\theta_1 \sin 2\theta_2 C_\chi}{2 I_{ex} S_{\theta 1}^{\,2} S_{\theta 2}^{\,2}}$$

A.5 Nonlinear Top-Nonlinear Top ($n = 8$). Moments of inertia − Fragment 1: I_{1a}, I_{1b}, I_{1c} Fragment 2: I_{2a}, I_{2b}, I_{2c} (see Chart 1 for $\mathbf{A}_r^0$)

$$\dot{\mathbf{Q}}_{cm,r}^{T} \; (\omega_x, \omega_y, \omega_z, \dot{\theta}_1, \dot{\phi}_1, \dot{\theta}_2, \dot{\phi}_2, \dot{\chi})$$

$$|\mathbf{A}_r^{\,0}| = S_{\theta 1}^{\,2} S_{\theta 2}^{\,2} I_{ex}^{\,2} I_{1a} I_{1b} I_{1c} I_{2a} I_{2b} I_{2c}$$

where

$$\Sigma_i^{\,+} = I_{ib} C_{\phi i}^{\,2} + I_{ic} S_{\phi i}^{\,2}$$

$$\Sigma_i^{\,-} = I_{ib} S_{\phi i}^{\,2} + I_{ic} C_{\phi i}^{\,2}$$

$$\Delta_{Ci} = (I_{ic} - I_{ib}) C_{\theta i} C_{\phi i} S_{\phi i}$$

$$\Delta_{Si} = (I_{ic} - I_{ib}) S_{\theta i} C_{\phi i} S_{\phi i}$$

$$\Pi = (\Sigma_2^{\,-} - I_{2a}) C_{\theta 2} S_{\theta 2}$$

$$I_{xx} = I_{1a} S_{\theta 1}^{\,2} + \Sigma_1^{\,-} C_{\theta 1}^{\,2} + (I_{2a} S_{\theta 2}^{\,2} + \Sigma_2^{\,-} C_{\theta 2}^{\,2}) C_\chi^{\,2} - 2\Delta_{C2} C_\chi S_\chi + \Sigma_2^{\,+} S_\chi^{\,2} + I_{ex}$$

$$I_{xy} = \Delta_{C1} + \Delta_{C2}(2C_\chi^{\,2} - 1) + (\Sigma_2^{\,-} C_{\theta 2}^{\,2} - \Sigma_2^{\,+} + I_{2a} S_{\theta 2}^{\,2}) S_\chi C_\chi$$

$$I_{xz} = (\Sigma_1^{\,-} - I_{1a}) C_{\theta 1} S_{\theta 1} - \Delta_{S2} S_\chi + (\Sigma_2^{\,-} - I_{2a}) C_{\theta 2} S_{\theta 2} C_\chi$$

$$I_{yy} = \Sigma_1^{\,+} + \Sigma_2^{\,+} C_\chi^{\,2} + I_{2a} S_{\theta 2}^{\,2} S_\chi^{\,2} + \Sigma_2^{\,-} C_{\theta 2}^{\,2} S_\chi^{\,2} + 2\Delta_{C2} C_\chi S_\chi + I_{ex}$$

$$I_{yz} = \Delta_{S1} + \Delta_{S2} C_\chi + (\Sigma_2^{\,-} - I_{2a}) C_{\theta 2} S_{\theta 2} S_\chi$$

$$I_{zz} = \Sigma_1^{\,-} S_{\theta 1}^{\,2} + I_{1a} C_{\theta 1}^{\,2} + \Sigma_2^{\,-} S_{\theta 2}^{\,2} + I_{2a} C_{\theta 2}^{\,2}$$

CHART 1

$$\mathbf{A}_r^0 = \begin{bmatrix} I_{xx} & I_{xy} & I_{xz} & -I_{1a}S_{\theta 1} & \Delta_{C1} & -I_{2a}S_{\theta 2}C_\chi & \Delta_{C2}C_\chi - \Sigma_2^+ S_\chi & \Pi C_\chi - \Delta_{S2}S_\chi \\ I_{xy} & I_{yy} & I_{yz} & 0 & \Sigma_1^+ & -I_{2a}S_{\theta 2}S_\chi & \Delta_{C2}S_\chi + \Sigma_2^+ C_\chi & \Pi S_\chi + \Delta_{S2}C_\chi \\ I_{xz} & I_{yz} & I_{zz} & I_{1a}C_{\theta 1} & \Delta_{S1} & I_{2a}C_{\theta 2} & \Delta_{S2} & \Sigma_2^- S_{\theta 2}^2 + I_{2a}C_{\theta 2}^2 \\ -I_{1a}S_{\theta 1} & 0 & I_{1a}C_{\theta 1} & I_{1a} & 0 & 0 & 0 & 0 \\ \Delta_{C1} & \Sigma_1^+ & \Delta_{S1} & 0 & \Sigma_1^+ & 0 & 0 & 0 \\ -I_{2a}S_{\theta 2}C_\chi & -I_{2a}S_{\theta 2}S_\chi & I_{2a}C_{\theta 2} & 0 & 0 & I_{2a} & 0 & I_{2a}C_{\theta 2} \\ \Delta_{C2}C_\chi - \Sigma_2^+ S_\chi & \Delta_{C2}S_\chi + \Sigma_2^+ C_\chi & \Delta_{S2} & 0 & 0 & 0 & \Sigma_2^+ & \Delta_{S2} \\ \Pi C_\chi - \Delta_{S2}S_\chi & \Pi S_\chi + \Delta_{S2}C_\chi & \Sigma_2^- S_{\theta 2}^2 + I_{2a}C_{\theta 2}^2 & 0 & 0 & I_{2a}C_{\theta 2} & \Delta_{S2} & \Sigma_2^- S_{\theta 2}^2 + I_{2a}C_{\theta 2}^2 \end{bmatrix}$$

Inverse elements

$$(G_r^0)_{44} = \frac{1}{I_{ex}S_{\theta 1}^2} + \frac{1}{I_{1a}} + \frac{C_{\theta 1}^2}{S_{\theta 1}^2}\left(\frac{S_{\phi 1}^2}{I_{1b}} + \frac{C_{\phi 1}^2}{I_{1c}}\right)$$

$$(G_r^0)_{45} = \frac{\Delta_{C1}}{I_{1b}I_{1c}S_{\theta 1}}$$

$$(G_r^0)_{46} = \frac{C_\chi}{I_{ex}S_{\theta 1}S_{\theta 2}}$$

$$(G_r^0)_{47} = \frac{S_\chi}{I_{ex}S_{\theta 1}}$$

$$(G_r^0)_{48} = \frac{C_{\theta 1}}{I_{ex}S_{\theta 1}^2} + \frac{C_{\theta 1}}{S_{\theta 1}^2}\left(\frac{S_{\phi 1}^2}{I_{1b}} + \frac{C_{\phi 1}^2}{I_{1c}}\right) - \frac{C_{\theta 2}C_\chi}{I_{ex}S_{\theta 1}S_{\theta 2}}$$

$$(G_r^0)_{55} = \frac{S_{\phi 1}^2 I_{1b} + C_{\phi 1}^2 I_{1c}}{I_{1b}I_{1c}} + \frac{1}{I_{ex}}$$

$$(G_r^0)_{56} = \frac{S_\chi}{I_{ex}S_{\theta 2}}$$

$$(G_r^0)_{57} = \frac{C_\chi}{I_{ex}}$$

$$(G_r^0)_{58} = \frac{C_{\theta 2}S_\chi}{I_{ex}S_{\theta 2}} + \left(\frac{1}{I_{1b}} - \frac{1}{I_{1c}}\right)\frac{C_{\phi 1}S_{\phi 1}}{S_{\theta 1}}$$

$$(G_r^0)_{66} = \frac{1}{I_{ex}S_{\theta 2}^2} + \frac{1}{I_{2a}} + \frac{C_{\theta 2}^2}{S_{\theta 2}^2}\left(\frac{S_{\phi 2}^2}{I_{2b}} + \frac{C_{\phi 2}^2}{I_{2c}}\right)$$

$$(G_r^0)_{67} = \frac{\Delta_{2c}}{I_{2b}I_{2c}S_{\theta 2}}$$

$$(G_r^0)_{68} = \frac{C_{\theta 2}}{I_{ex}S_{\theta 2}^2} + \frac{C_{\theta 2}}{S_{\theta 2}^2}\left(\frac{S_{\phi 2}^2}{I_{2b}} + \frac{C_{\phi 2}^2}{I_{2c}}\right) - \frac{C_{\theta 1}C_\chi}{I_{ex}S_{\theta 1}S_{\theta 2}}$$

$$(G_r^0)_{77} = \frac{S_{\phi 2}^2 I_{2b} + C_{\phi 2}^2 I_{2c}}{I_{2b}I_{2c}} + \frac{1}{I_{ex}}$$

$$(G_r^0)_{78} = \frac{C_{\theta 1}S_\chi}{I_{ex}S_{\theta 1}} + \left(\frac{1}{I_{2b}} - \frac{1}{I_{2c}}\right)\frac{C_{\phi 2}S_{\phi 2}}{S_{\theta 2}}$$

$$(G_r^0)_{88} = \frac{1}{S_{\theta 1}^2}\left(\frac{S_{\phi 1}^2}{I_{1b}} + \frac{C_{\phi 1}^2}{I_{1c}}\right) + \frac{1}{S_{\theta 2}^2}\left(\frac{S_{\phi 2}^2}{I_{2b}} + \frac{C_{\phi 2}^2}{I_{2c}}\right) + \frac{1 - \cos 2\theta_1 \cos 2\theta_2 + \sin 2\theta_1 \sin 2\theta_2 C_\chi}{2I_{ex}S_{\theta 1}^2 S_{\theta 2}^2}$$

B. Derivation of Final Expression for *F*. The necessary relationships among the sines and cosines of the sets of angles (γ_i, δ_i) and (α_i, β_i, θ_i, ϕ_i, χ), ($i = 1, 2$) are explicitly derived for two nonlinear tops. This is worked out first for reactant 1 with reference to Figure 2; the analogous derivation for reactant 2 follows.

In the internal coordinate system of fragment 1, $\mathbf{d}_1$ by definition is characterized by (α_1,β_1). With some consideration of Figure 2, it becomes clear that the z axis of the collision system can be characterized in the internal coordinate system by (θ_1, $\pi - \phi_1$). The addition of spherical angles then gives

$$\cos\gamma_1 = \cos\alpha_1 \cos\theta_1 - \sin\alpha_1 \sin\theta_1 \cos(\beta_1 + \phi_1) \quad \text{(B1)}$$

In the collision coordinate system translated to the center of mass of reactant 1, the spherical polar angles for the internal z-axis are (θ_1, 0). Equation B1 determines the spherical angle γ_1 for $\mathbf{d}_1$ leaving the polar angle δ_1. The angle between the internal z axis and $\mathbf{d}_1$ is α_1. The addition of spherical angles gives

$$\cos\delta_1 = (\cos\alpha_1 - \cos\gamma_1 \cos\theta_1)/\sin\gamma_1 \sin\theta_1 \quad \text{(B2)}$$

In this equation, substitution of eq B1 for $\cos\gamma_1$ gives

$$\cos\delta_1 = (\cos\alpha_1 \sin\theta_1 + \sin\alpha_1 \cos\theta_1 \cos(\beta_1 + \phi_1))/\sin\gamma_1 \quad \text{(B3)}$$

Furthermore, via eqs B1 and B3, one obtains

$$\sin\delta_1 = [1 - \cos^2\delta_1]^{1/2} = \sin\alpha_1 \sin(\beta_1 + \phi_1)/\sin\gamma_1 \quad \text{(B4)}$$

For reactant 2, upon some consideration of Figure 1, it becomes clear that the angle γ_2 between the collision-system z-axis and $\mathbf{d}_2$ is independent of χ and therefore χ can be set to zero. Therefore

$$\cos\gamma_2 = \cos\alpha_2 \cos\theta_2 - \sin\alpha_2 \sin\theta_2 \cos(\beta_2 + \phi_2) \quad \text{(B5)}$$

In the collision coordinate system translated to the center of mass of reactant 2, the angles for the internal z-axis of fragment 2 are known, i.e., (θ_2, χ). Equations B3 and B4 then apply if δ_1 is changed to $\delta_2 - \chi$. However, eqs B3 and B4 and their analogues for reactant 2 are not directly needed in F but rather the product $\sin\gamma_1 \sin\gamma_2 \cos(\delta_1 - \delta_2)$. After the necessary

substitutions, that product assumes the form

$$\sin\gamma_1 \sin\gamma_2 \cos(\delta_1 - \delta_2) = [\{\cos\alpha_1 \sin\theta_1 + \sin\alpha_1 \cos\theta_1 \cos(\beta_1 + \phi_1)\}\{\cos\alpha_2 \sin\theta_2 + \sin\alpha_2 \cos\theta_2 \cos(\beta_2 + \phi_2)\} - \sin\alpha_1 \sin(\beta_1 + \phi_1)\sin\alpha_2 \sin(\beta_2 + \phi_2)]\cos\chi + [\sin\alpha_1 \sin(\beta_1 + \phi_1)\{\cos\alpha_2 \sin\theta_2 + \sin\alpha_2 \cos\theta_2 \cos(\beta_2 + \phi_2)\} + \sin\alpha_2 \sin(\beta_2 + \phi_2)\{\cos\alpha_1 \sin\theta_1 + \sin\alpha_1 \cos\theta_1 \cos(\beta_1 + \phi_1)\}]\sin\chi \quad \text{(B6)}$$

Substitution of eqs B1, B5, and B6 into eq 17 results in an F expression explicit in its dependence on all of θ_1, ϕ_1, θ_2, ϕ_2, χ, d_1, α_1, β_1, d_2, α_2, β_2, and R.

References and Notes

(1) Wagner, A. F.; Harding, L. B.; Robertson, S. H.; Wardlaw, D. M. *Ber. Bunsunges. Phys. Chem.* **1997**, *101*, 391.
(2) Klippenstein, S. J.; Allen, W. D. *Ber. Bunsunges. Phys. Chem.* **1997**, *101*, 423.
(3) Troe, J. *Ber. Bunsunges. Phys. Chem.* **1997**, *101*, 438.
(4) Klippenstein, S. J.; Harding, L. B. *Phys. Chem. Chem. Phys.* **1999**, *1*, 989.
(5) Smith, S. C. *J. Chem. Phys.* **1999**, *111*, 1830.
(6) Wardlaw, D. M.; Marcus, R. A. *Adv. Chem. Phys.* **1988**, *70*, 231, part 1.
(7) Klippenstein, S. J. *J. Chem. Phys.* **1992**, *96*, 367.
(8) Klippenstein, S. J. *J. Chem. Phys.* **1993**, *99*, 3644.
(9) Klippenstein, S. J. *J. Phys. Chem.* **1994**, *98*, 11459.
(10) Wardlaw, D. M.; Marcus, R. A. *Chem. Phys. Lett.* **1984**, *110*, 230; *J. Chem. Phys.* **1985**, *83*, 3462.
(11) Robertson, S. H.; Wagner, A. F.; Wardlaw, D. M. *J. Chem. Phys.* **1995**, *103*, 2917.
(12) Robertson, S. H.; Wagner, A. F.; Wardlaw, D. M. *Faraday Discuss. Chem. Soc.* **1995**, *102*, 65.
(13) Robertson, S. H.; Wagner, A. F.; Wardlaw, D. M. *J. Chem. Phys.* **2000**, *113*, 2648.
(14) Klippenstein, S. J.; Wagner, A. F.; Robertson, S. H.; Dunbar, R.; Wardlaw, D. M. *VariFlex Software, Version 1.0* 1999. This software is available at no charge and includes a user manual; see the VariFlex web site (http://chemistry.anl.gov/variflex) for instructions on downloading and installation.
(15) Klippenstein, S. J.; Harding, L. B. *J. Phys. Chem. A* **2000**, *104*, 2351.
(16) Mayo, S. L.; Olafson, B. D.; Goddard, W. A. *J. Phys. Chem.* **1990**, *94*, 8897.
(17) Chase, M. W., Jr.; Davies, C. A.; Downey, J. R., Jr.; Frurip, D. J.; McDonald, R. A.; Syverud, A. N. *J. Phys. Chem. Ref. Data 14* **1985**, Suppl. 1.
(18) Kurylo, M. J.; Howard, C. C. C. J.; Ravishankara, A. R.; Kolb, C. E.; Molina, M. J. *Chemical Kinetics and Photochemical Data for Use in Stratospheric Modeling*, Evaluation No. 11, JPL Publication 94-26, Dec. 15, 1994.
(19) Harding, L.B. Argonne National Laboratory, private communication.
(20) Wardlaw, D. M.; Marcus, R. A. *J. Phys. Chem.* **1986**, *90*, 5383.
(21) Aubanel, E. E.; Wardlaw, D. M. *J. Phys. Chem.* **1989**, *93*, 3117.
(22) MAPLE, *Waterloo Maple Software*, University of Waterloo, Waterloo, Onatrio, 1991.